Journal of Infrastructure Intelligence and Resilience 5 (2026) 100253

Contents lists available at ScienceDirect

Journal of Infrastructure Intelligence and Resilience

journal homepage: www.journals.elsevier.com/journal-of-infrastructure-intelligence-and-resilience

An open-source framework for coupled vehicle–bridge interaction analysis using OpenSees

Mohammad Talebi-Kalaleh, Qipei Mei *

Department of Civil and Environmental Engineering, University of Alberta, Edmonton, Canada

ARTICLE INFO

Dataset link: https://github.com/MTalebi/OpenSees-VBI-Simulation

Keywords:
Vehicle–bridge interaction
OpenSees
Iterative partitioned coupling
Moving mass
Drive-by bridge monitoring

ABSTRACT

Vehicle–bridge interaction (VBI) analysis simulates bridge response under moving vehicles, with applications in dynamic amplification, weigh-in-motion, and drive-by bridge monitoring. VBI theory is mature, but most implementations are custom research codes that are hard to reuse. This paper presents an open-source Python framework for VBI analysis built on OpenSees. Separate OpenSees bridge and vehicle models exchange axle displacements and contact forces at every time step through iterative partitioned coupling. The linear bridge model accepts vertical support springs and prescribed external loads; richer substructures need additional state and interface handling. Sampled axle trajectories accommodate time-varying speed. Five vehicle models range from a single-axle spring-mass system to a two-axle composite half-car with body pitch. A decoupled mode applies the vehicle weight as a moving force, then excites the vehicle with the resulting bridge motion. The implementation is numerically verified on three published benchmark configurations against independent reference solutions and published results, with $R^2 \geq 0.9997$ and peak-response errors of at most 0.14 %. A parametric study maps the coupled-decoupled agreement over the vehicle-to-bridge mass and frequency ratios, span length, speed, roughness, and background traffic, with Monte Carlo repetitions over roughness and traffic realisations. The mass ratio governs the discrepancy only when the vehicle frequency is well below the bridge frequency; near frequency tuning, the decoupled mode misrepresents the dynamic bridge and vehicle responses even for light vehicles. Response-specific screening targets are reported for the sampled combinations. The framework source code and vehicle configurations are available through a public repository.

1. Introduction

The dynamic interaction between moving vehicles and bridges has been studied in structural engineering for more than half a century (Frýba, 1999; Yang et al., 2004b). When a vehicle crosses a bridge, the coupled response of the two subsystems can differ considerably from what a simpler constant- or moving-force model would predict. Vehicle–bridge interaction (VBI) analysis is the modelling basis for several engineering problems: the estimation of dynamic amplification factors for bridge design and assessment, bridge weigh-in-motion (B-WIM), in which axle loads are inferred from measured bridge response, and indirect (drive-by) bridge monitoring, in which bridge condition is inferred from the response of an instrumented vehicle passing over the bridge (Malekjafarian et al., 2015; Yang et al., 2004a).

The theoretical foundation of VBI goes back to Frýba (1999), who derived analytical solutions for beams subjected to moving forces and moving masses. Yang et al. (2004b) later developed a VBI finite element in which the vehicle degrees of freedom are condensed into the bridge element matrices at the contact points, giving a monolithic solution of the coupled system. The formulation was extended to asymmetric two-axle (half-car) vehicles with body pitch by Yang et al. (2019) and has since served as a standard reference for validating VBI implementations. In parallel, Green and Cebon (1994) and Zhu and Law (2002), and others developed iterative partitioned coupling as an alternative to the monolithic approach. In a partitioned scheme the bridge and the vehicle are solved as independent subsystems and the contact forces and displacements are exchanged iteratively at each time step until they converge. The partitioned approach is more flexible because each subsystem can use its own solver, mesh, and time integration scheme.

These applications cover both forward simulation (for design and dynamic amplification studies) and inverse analysis (for B-WIM and condition assessment). On the forward side, VBI models underpin the dynamic impact factors used in bridge design and assessment, from the early multi-girder studies of Huang et al. (1992) to the traffic-based factors of Deng and Cai (2010) and the review of Deng et al. (2015); they are also the engine of traffic-load simulation, in which measured or synthetic traffic streams are driven across bridge models to obtain

* Corresponding author.
E-mail address: qipei.mei@ualberta.ca (Q. Mei).

https://doi.org/10.1016/j.iintel.2026.100253
Received 12 August 2026; Received in revised form 6 October 2026; Accepted 10 October 2026
Available online 21 October 2026
2772-9915/© 2026 The Authors. Published by Elsevier Ltd on behalf of Zhejiang University and Zhejiang University Press Co., Ltd. This is an open access article under the CC BY-NC-ND license (http://creativecommons.org/licenses/by-nc-nd/4.0/).

Nomenclature

Symbol	Meaning
L	Bridge span length
E, I, A	Elastic modulus, second moment of area, cross-sectional area of the beam
$\bar{m}$	Bridge mass per unit length
ζ	Bridge damping ratio (Rayleigh, anchored at the first two modes)
N_e, N_n	Number of beam elements and nodes ($N_n = N_e + 1$)
Δx, Δt	Beam element length and integration time step
$w(x,t)$	Bridge vertical deflection field
$r(x)$	Road roughness profile
$u_c(t)$	Contact-point displacement, $u_c = w(x_a(t),t) + r(x_a(t))$
$x_a(t)$	Axle position along the bridge
v	Vehicle speed
m_v, J_v	Vehicle body mass and pitch moment of inertia
m_s, m_u	Sprung (body) and unsprung (axle) masses of the quarter-car
k_s, c_s	Suspension stiffness and damping
k_t, c_t	Tyre stiffness and damping
k_f, c_f, k_r, c_r	Front and rear suspension stiffness and damping (half-car)
d	Axle spacing ($d = d_1 + d_2$)
d_1, d_2	Distance from the body centre of gravity to the front and rear axle
y_v, θ_v	Body bounce displacement and pitch rotation
F_c, F_r, F_f	Contact force; rear and front axle contact forces
$G_d(n)$	Displacement PSD of road roughness at spatial frequency n
n_0	Reference spatial frequency, 0.1 cycles/m
Δn, n_l, n_u	Spatial frequency increment and band limits of the roughness synthesis
μ	Vehicle-to-bridge mass ratio, $\mu = m_v/(\bar{m}L)$
f_1, ω_1	First natural frequency of the bridge (Hz, rad/s)
S	Dimensionless speed parameter, $S = v/(2f_1L)$
f_v, f_{bounce}, f_{hop}	vehicle natural frequency; body-bounce and axle-hop frequencies of the quarter-car
r	Vehicle-to-bridge frequency ratio, $r = f_v/f_1$
ζ_s	Suspension damping ratio referred to the sprung mass
$\mathbf{F}_{\text{ext}}(t)$	External nodal force history applied to the bridge (background traffic in this paper)
k_{sup}	Vertical stiffness of a flexible support (bearing, pier, or foundation)
$\epsilon^{(k)}$	Normalised displacement residual at coupling iteration k
ϵ_{tol}	Convergence tolerance of the iterative coupling
R^2	Coefficient of determination
NRMSE	Root-mean-square error normalised by the reference signal range

extreme effects (Enright and O'Brien, 2013; O'Brien and Enright, 2011), and they explain the transient shifts of bridge frequencies observed during truck passages (Cantero et al., 2017). On the inverse side, B-WIM has grown from Moses' influence-line algorithm (Moses, 1979) to systems that calibrate the influence line from measurements (O'Brien et al., 2006), resolve transverse wheel-load distribution (Zhao et al., 2014), and are reviewed in Lydon et al. (2016), Yu et al. (2016), and Paul and Roy (2023); moving-load and parameter identification from bridge response is reviewed by Zhu and Law (2016). Among the inverse applications, drive-by (indirect) monitoring has driven much of the recent activity in VBI simulation. Yang et al. (2004a) first showed that bridge natural frequencies appear in the spectrum of a passing vehicle's acceleration, which Lin and Yang (2005) confirmed experimentally. Subsequent work extended the idea to damping identification (González et al., 2012; Keenahan et al., 2014), mode-shape estimation (Kong et al., 2016; Malekjafarian and O'Brien, 2017; Yang et al., 2014), contact-point responses that suppress the vehicle's own dynamics (Yang et al., 2018), damage detection from apparent profiles and displacement differences (Elhattab et al., 2016; Kim and Kawatani, 2008; O'Brien et al., 2014; O'Brien and Keenahan, 2015), the combination of moving and stationary sensors (Li et al., 2019), and learning-based detectors trained on simulated fleets (Cantero et al., 2024; Corbally and Malekjafarian, 2022; Sarwar and Cantero, 2021). Hester and González (2017) give a critical account of what drive-by data can and cannot resolve. Crowdsourced smartphone sensing has extended the concept to ordinary traffic (Matarazzo et al., 2018, 2022; Shirzad-Ghaleroudkhani and Gül, 2020; Talebi-Kalaleh and Mei, 2023, 2024), and (Sadeghi Eshkevari et al., 2020a) and (Mei et al., 2019, 2021) developed modal identification and damage detection pipelines for such data; the field is reviewed in Malekjafarian et al. (2015), Yang and Yang (2018), Yang et al. (2020), and Malekjafarian et al. (2022). Recent experimental and sensing developments sharpen the requirements on such models. Gkoktsi et al. (2024) tested drive-by monitoring on a full-scale short bridge while characterising both vehicle and bridge dynamics. Irawan et al. (2025) tested a revised virtual-axle damage indicator using laboratory BWIM measurements. The review of Gao et al. (2026) distinguishes vision-based vehicle weighing from bridge-response-based weighing and identifies environmental robustness and measurement accuracy as continuing challenges. These developments require accurate vehicle dynamics and contact-force histories as well as bridge deflection; agreement in peak deflection alone does not establish suitability for monitoring or weighing.

All of these methods need a VBI model with enough fidelity for both their development and their validation, and most published studies have relied on purpose-built simulators.

VBI is equally central beyond highway bridges under ordinary traffic. Train-track-bridge interaction has its own extensive literature, with three-dimensional multi-body train models, track layers, and nonlinear wheel-rail contact (Antolín et al., 2013; Cheng et al., 2001; Dimitrakopoulos and Zeng, 2015; Montenegro et al., 2015; Xia and Zhang, 2005; Zhai et al., 2013); Zhai et al. (2019) review the state of the art. Coupled vehicle-bridge-wind analysis (Cai and Chen, 2004; Xu and Guo, 2003) and vehicle–bridge response during earthquakes (Kim et al., 2011; Zeng and Dimitrakopoulos, 2016) add environmental excitation to the same coupled system, and lumped-parameter soil models have been attached to the bridge supports to capture structure–soil interaction (Bucinskas and Andersen, 2020). On the mechanics side, Stoura and Dimitrakopoulos (2020a,c,b) showed that the interaction acts on the bridge as additional damping, stiffness, and loading terms whose magnitude is governed by the vehicle-to-bridge frequency ratio as well as by the mass ratio, and proposed a dynamic partitioning scheme for the coupled problem (Neves et al., 2012; Stoura et al., 2021) formulated a direct (non-iterative) treatment of the contact constraint, and Sadeghi Eshkevari et al. (2020b) quantified when a decoupled (moving-load) simplification is acceptable for medium- to long-span bridges. The framework presented here targets general VBI analysis

rather than a single application, so the same code can be used for design, B-WIM and monitoring studies, and the partitioned architecture offers a route to richer models; the released solver demonstrates only the linear planar cases described below.

Although the theory is mature, implementation is still a practical barrier. Most VBI codes are written from scratch using custom finite elements or analytical modal superposition, which requires considerable computational mechanics expertise. Such codes are usually maintained inside a single research group and are rarely shared as reusable and documented software. At the same time, general-purpose finite element packages such as OpenSees (McKenna, 2011), which are widely used in structural engineering, have no built-in support for moving load or moving mass analysis.

This paper addresses that gap with an open-source Python framework that performs VBI analysis on top of OpenSees. The bridge and the vehicle are built as separate OpenSees models with standard elements (`elasticBeamColumn` for the bridge, and `zeroLength` or `twoNodeLink` spring-dashpot elements for the vehicle), and they are coupled externally through an iterative Python algorithm. No change to the OpenSees source code and no custom element are required. At every time step, the bridge deflection at each axle is added to the road roughness, the resulting displacement is imposed on the vehicle, the axle reactions are computed and mapped back to the bridge nodes, the bridge is re-solved, and the loop repeats until the bridge response converges.

The principal contribution is a reusable OpenSeesPy implementation of established partitioned VBI coupling, rather than a new coupling algorithm or new vehicle equations (González, 2010; Green and Cebon, 1994; Stoura et al., 2021; Zhu and Law, 2002). The software integrates five standard vehicle topologies, linear bridge models, roughness generation, prescribed axle trajectories, and coupled and decoupled solution modes using ordinary OpenSees elements. The rebuild strategy passes nodal kinematic states between successive solves; it supports the linear-elastic subsystems studied here, but does not preserve nonlinear material history (Section 6.4). The accompanying numerical contributions are checks of the three benchmark configurations against independent reference solutions and published results, and a controlled study of mass and frequency ratios, supplemented by Monte Carlo checks for two quarter-car configurations. These results provide response-specific screening guidance within the tested domain, rather than a universal criterion for all bridges and vehicle classes. The release includes the model inputs, numerical outputs, and reproduction scripts.

The rest of the paper is organised as follows. Section 2 reviews the theoretical background and the existing numerical approaches to VBI. Section 3 describes the framework, including the bridge and vehicle finite element models, the iterative coupling algorithm, the road roughness model, and the decoupled mode. Section 4 verifies the framework numerically on three published benchmark configurations. Section 5 reports a parametric study that compares the coupled and decoupled modes across the main problem parameters. Section 6 discusses the main observations and limitations, and Section 7 concludes.

2. Literature review

2.1. Analytical foundations

The simplest dynamic loading model treats the vehicle as a constant force moving at speed v. Frýba (1999) derived closed-form modal-superposition solutions for this case. Because the model ignores the vehicle inertia, it cannot capture the feedback between vehicle vibration and bridge deformation, which is the key feature of the vehicle–bridge interaction (VBI) problem.

The VBI formulation has two coupled mechanisms. First, the vehicle is base-excited: each axle follows the bridge surface, whose vertical profile is the sum of the structural deflection $w(x,t)$ and the road roughness $r(x)$. The contact-point displacement is

$$u_c(t) = w\big(x_a(t),\, t\big) + r\big(x_a(t)\big) \tag{1}$$

where $x_a(t)$ is the axle position, and it drives the vehicle equations of motion from below. Second, the bridge sees the vehicle as a moving dynamic load: the spring, dashpot, and inertial forces transmitted at each contact point act as time-varying nodal forces on the beam. Because the bridge deflection depends on the vehicle forces and the vehicle forces depend on the bridge deflection, the two subsystems must be solved together at each time step. Fig. 1 illustrates the coupled problem for a two-axle vehicle crossing a simply supported beam.

2.2. Vehicle models

The framework provides five vehicle model types of increasing complexity. Four representative configurations are shown in Fig. 2; a fifth variant with two independent sprung/unsprung pairs and no body pitch is documented in Appendix. All models are driven by the contact-point displacement u_c defined in Eq. (1), and they all transmit a contact force back to the bridge equal to the reaction at the constrained axle node. The contact (wheel) nodes themselves carry no degrees of freedom: their vertical displacement and velocity are prescribed from the bridge motion and the road profile, exactly as the supports in a multiple-support excitation analysis, and the dynamic DOFs of each model are those of the masses above the contact (Table 11 in the Appendix). The governing equations are given below. The static contribution of gravity is computed once at the start of the analysis and is left out of the dynamic equations that follow.

The **single-axle simple model** (Fig. 2a) represents the vehicle as a lumped mass m connected to the contact point through a spring k and dashpot c. With the mass displacement denoted y, the equation of motion is

$$m\,\ddot{y} + c\,\dot{y} + k\,y = c\,\dot{u}_c + k\,u_c \tag{2}$$

and the contact force transmitted to the bridge is $F_c = k(y-u_c)+c(\dot{y}-\dot{u}_c)$. Yang et al. (2004b) used this model to derive analytical VBI solutions and to validate finite element formulations.

The **quarter-car model** (Fig. 2b) splits the vehicle into a sprung mass m_s (the body) and an unsprung mass m_u (the axle/wheel assembly), joined by the suspension (k_s, c_s). The axle is in turn connected to the contact point through the tyre (k_t, c_t). The two-DOF model captures both the low-frequency body bounce and the higher-frequency axle hop, and it is the standard model in drive-by bridge monitoring studies (O'Brien and Keenahan, 2015; Sadeghi Eshkevari et al., 2020a). The equations of motion are

$$\begin{bmatrix} m_u & 0 \\ 0 & m_s \end{bmatrix} \begin{Bmatrix} \ddot{y}_u \\ \ddot{y}_s \end{Bmatrix} + \begin{bmatrix} c_t + c_s & -c_s \\ -c_s & c_s \end{bmatrix} \begin{Bmatrix} \dot{y}_u \\ \dot{y}_s \end{Bmatrix} + \begin{bmatrix} k_t + k_s & -k_s \\ -k_s & k_s \end{bmatrix} \begin{Bmatrix} y_u \\ y_s \end{Bmatrix} = \begin{Bmatrix} c_t\,\dot{u}_c + k_t\,u_c \\ 0 \end{Bmatrix} \tag{3}$$

where y_u and y_s are the axle and body displacements. Only the tyre layer connects to the bridge, so the contact force is $F_c = k_t(y_u - u_c) + c_t(\dot{y}_u - \dot{u}_c)$.

The **half-car model with pitch** (Fig. 2c) extends the formulation to two-axle vehicles. The body has mass m_v and pitch moment of inertia J_v; it has a vertical translation y_v and a rotation θ_v about its centre of gravity (CG). The rear and front suspensions (k_r, c_r and k_f, c_f) connect the body directly to the two contact points, without separate axle masses. Let d_1 be the distance from the CG to the front axle, d_2 the distance from the CG to the rear axle (Fig. 2c), and u_{cr} and u_{cf} the rear and front contact-point displacements. The bounce equation is

$$m_v\ddot{y}_v + (c_r + c_f)\dot{y}_v + (k_r + k_f)y_v + (d_1 c_f - d_2 c_r)\dot{\theta}_v + (d_1 k_f - d_2 k_r)\theta_v = k_r u_{cr} + k_f u_{cf} + c_r\dot{u}_{cr} + c_f\dot{u}_{cf} \tag{4}$$

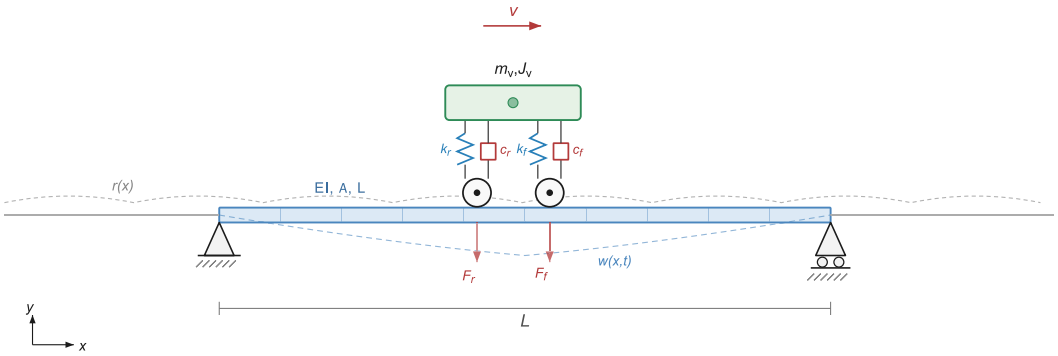

Fig. 1. Schematic of the vehicle–bridge interaction problem. A multi-DOF vehicle traverses an Euler–Bernoulli beam bridge at velocity v, with interaction forces F_r and F_f transmitted at the rear and front axle positions through shape function interpolation.

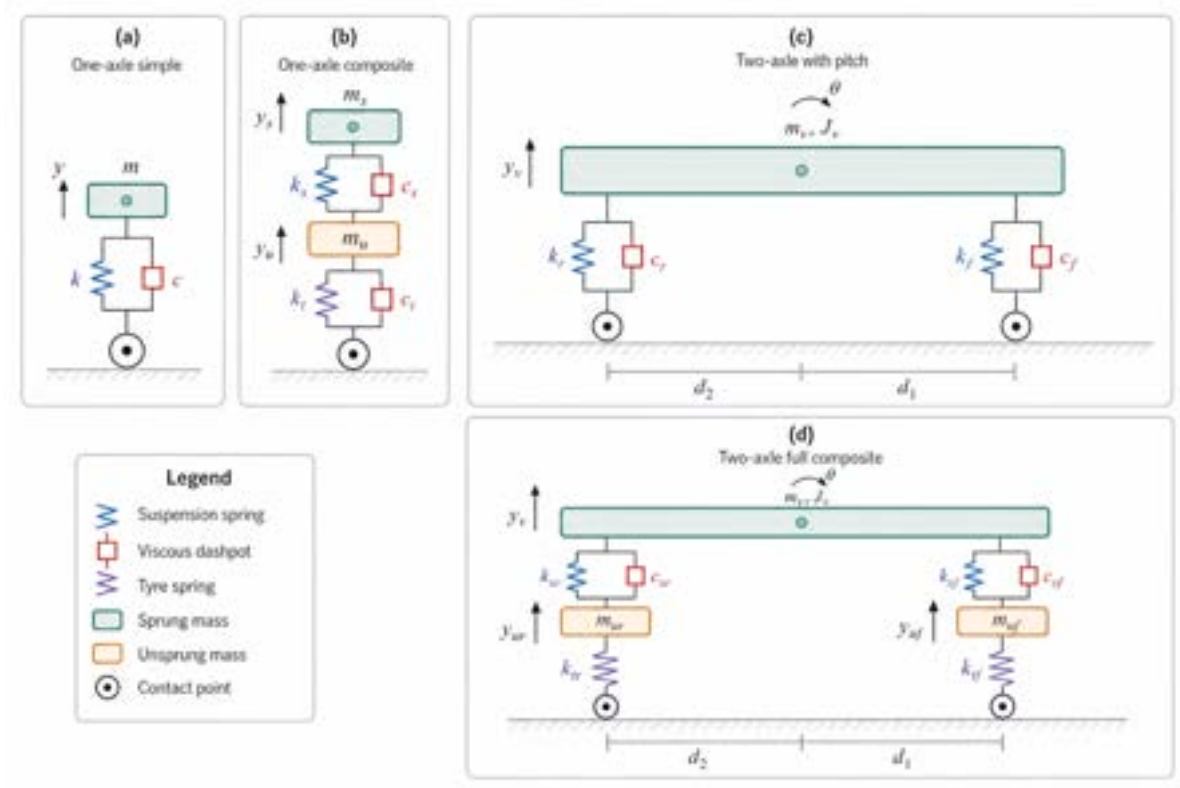

Fig. 2. Vehicle models supported by the framework: (a) single-axle simple, (b) quarter-car composite, (c) half-car with pitch, and (d) full composite half-car with axle masses. The small circular markers at the road surface are the contact (wheel) nodes: their vertical motion is prescribed by Eq. (1), so they carry no mass and no dynamic degree of freedom, and the contact force is the reaction at the prescribed node. In (a) and (c) the spring-dashpot connects the body directly to the contact node; in (b) and (d) the unsprung (axle) mass is a separate node above the contact node, connected to it through the tyre spring-dashpot.

and the pitch equation is

$$\begin{aligned} &J_v\ddot{\theta}_v + (d_1c_f - d_2c_r)\dot{y}_v + (d_1k_f - d_2k_r)y_v + (d_2^2c_r + d_1^2c_f)\dot{\theta}_v \\ &\quad + (d_2^2k_r + d_1^2k_f)\theta_v \\ &= d_1k_fu_{cf} - d_2k_ru_{cr} + d_1c_f\dot{u}_{cf} \\ &\quad - d_2c_r\dot{u}_{cr} \end{aligned} \tag{5}$$

This formulation, used by Yang et al. (2019) in their VBI element, has two dynamic DOFs and two contact points. The rear and front contact forces are $F_r = k_r(y_v - d_2\theta_v - u_{cr}) + c_r(\dot{y}_v - d_2\dot{\theta}_v - \dot{u}_{cr})$ and $F_f = k_f(y_v + d_1\theta_v - u_{cf}) + c_f(\dot{y}_v + d_1\dot{\theta}_v - \dot{u}_{cf})$.

The **full composite half-car model** (Fig. 2d) adds independent unsprung masses m_{ur} and m_{uf} at the two axles, each with its own tyre assembly (k_{tr}, c_{tr} and k_{tf}, c_{tf}), giving four DOFs: two axle translations, body bounce, and pitch. The model captures the full dynamics of a two-axle truck, including the separate frequency ranges of tyre hop (~10–15 Hz) and body bounce (~1–3 Hz), and has been used by O'Brien et al. (2014) and Cantero et al. (2024).

2.3. Coupling methods

The coupled VBI equations can be solved monolithically or through partitioned iteration. In the monolithic approach the vehicle DOFs are embedded directly in the beam element formulation; Yang's VBI element (Yang et al., 2019; Yang and Yau, 1997) augments the standard beam element matrices with the vehicle mass, stiffness, and damping contributions evaluated at the current contact position. The monolithic solution is unconditionally stable and needs no iteration, but it requires changes to the element library and the global matrices have to be reassembled at every time step.

The partitioned approach, adopted in this work, treats the bridge and the vehicle as separate subsystems and exchanges forces and displacements through an external interface. Green and Cebon (1994) described such a scheme for highway bridge dynamics, Zhu and Law (2002) extended it to multi-lane decks, and González (2010) reviewed its finite element implementation; Stoura et al. (2021) recently recast it as a dynamic partitioning method with proven convergence properties, and Neves et al. (2012) showed that the contact constraint can also be enforced directly, without iteration, when both subsystems are assembled in one solver. The partitioned approach is more modular: each subsystem can use its own solver, mesh, and time step. The price is that iteration is needed within each time step to enforce equilibrium and compatibility at the contact points. VBI models of this kind also underpin work beyond forward simulation of intact structures: moving-load analysis of damaged, nonlinear bridges (Law and Zhu, 2004), dynamic impact factors for bridge evaluation under realistic traffic (Deng and Cai, 2010), and interaction-based structural health monitoring and parameter identification (Zhu and Law, 2015).

A third family of methods replaces the coupled problem by a modified bridge problem. Stoura and Dimitrakopoulos (2020c,b) showed that, for a vehicle idealised as a sprung mass, the interaction is equivalent to additional damping, stiffness, and loading terms acting on the bridge, and that these terms depend on the vehicle-to-bridge frequency ratio ω_v/ω_b as much as on the mass ratio: the additional damping is largest when the vehicle frequency is tuned to the bridge frequency (Stoura and Dimitrakopoulos, 2020a), in the same way that a tuned mass damper is most effective at tuning. This observation matters for the decoupled (moving-load) mode offered by the present framework, because it implies that a light vehicle whose suspension frequency is close to a bridge frequency can still alter the dynamic part of the bridge response appreciably. Section 5.2 examines the two ratios jointly.

In the present framework, convergence of the partitioned iteration is measured by the relative change in the bridge displacement field between successive iterations:

$$\varepsilon^{(k)} = \frac{\sqrt{\frac{1}{N_n}\sum_{j=1}^{N_n}\left(w_j^{(k)} - w_j^{(k-1)}\right)^2}}{\max_j |w_j^{(k)}|} < \epsilon_{\text{tol}} \tag{6}$$

where $w_j^{(k)}$ is the bridge displacement at node j in iteration k, N_n is the number of bridge nodes, and ϵ_{tol} is a user-specified tolerance (typically 10^{-4} to 10^{-12}).

The residual is normalised by the largest current nodal displacement, so the criterion is scale-free across the span lengths and stiffnesses considered. When the bridge is (nearly) at rest, before the vehicle enters, the denominator is guarded: if the maximum displacement is zero, the step is accepted directly, and for very small responses the absolute residual in the numerator is itself at machine-precision level, so the guard is not activated in practice. The convergence quantity can also be switched to the velocity field, which carries no quasi-static offset, through a user option.

2.4. Road roughness

Road surface roughness is one of the main excitation sources for both the vehicle and the bridge in VBI problems. The ISO 8608 standard (International Organization for Standardization, 2016) characterises road profiles through their displacement power spectral density (PSD), which is modelled as a function of the spatial frequency:

$$G_d(n) = G_d(n_0)\left(\frac{n}{n_0}\right)^{-w} \tag{7}$$

where n is the spatial frequency in cycles/m, $n_0 = 0.1$ cycles/m is the reference frequency, $w = 2$ is the waviness exponent, and $G_d(n_0)$ is the roughness coefficient that defines the road class. The ISO 8608 standard classifies road surfaces into categories A through H based on $G_d(n_0)$; Table 1 lists classes A–E.

Table 1
ISO 8608 road roughness classification at reference spatial frequency $n_0 = 0.1$ cycles/m. Roughness coefficients $G_d(n_0)$ in 10^{-6} m^3.

Class	Description	Lower limit	Geometric mean	Upper limit
A	Very good	–	16	32
B	Good	32	64	128
C	Average	128	256	512
D	Poor	512	1024	2048
E	Very poor	2048	4096	8192

Throughout the numerical studies, R1, R2, and R3 denote the input coefficients $G_0 = G_d(0.1\,\text{cycles/m}) = 1, 16, 256 \times 10^{-6}$ m^3, respectively. R1 lies below the class-A geometric mean, R2 is the class-A mean, and R3 is the class-C mean. They are roughness levels, not three distinct ISO classes. All quoted coefficients refer to the unfiltered target spectrum; the five-sample moving average used for the simulated profiles attenuates short wavelengths, as quantified in Section 4.5. The reported profiles therefore do not establish performance on class-E roads or at short-wavelength defects.

A synthetic road roughness profile is generated as a sum of harmonics with random phase angles:

$$r(x) = \sum_{i=1}^{N_h} \sqrt{2\,G_d(n_i)\,\Delta n}\,\cos(2\pi n_i x + \phi_i) \tag{8}$$

where ϕ_i are independent random phases uniformly distributed over $[0, 2\pi]$, Δn is the spatial frequency increment, and n_i ranges from a lower bound n_l to an upper bound n_u. In the implementation, $n_u = 10$ cycles/m so that wavelengths down to 0.1 m are captured, and Δn is chosen so that the period of the synthesised profile ($1/\Delta n$) exceeds at least twice the bridge span. This avoids artificial periodicity within the analysis window.

2.5. Numerical platforms for VBI

VBI simulations have been implemented in many different numerical environments. Commercial finite element packages such as ABAQUS, ANSYS, and LS-DYNA can carry full-vehicle and bridge models, but they usually require user-written subroutines for the iterative coupling, and their licensing makes open sharing of the benchmark configurations difficult. Research codes such as the VBI-2D MATLAB solver used to generate the NuBe dataset (Cantero, 2024) are well documented but are usually tied to specific vehicle topologies or solver choices. Open-source structural analysis platforms such as OpenSees (McKenna, 2011), accessible from Python through OpenSeesPy (Zhu et al., 2018), provide reusable building blocks for structural dynamics, but they do not include native moving-mass analysis or a built-in mechanism for coupling separate bridge and vehicle subsystems. The framework presented here addresses that gap: it builds on a widely used open-source platform and adds an external Python coupling layer that works with standard elements, so the complete VBI models and the benchmark cases can be shared, inspected, and extended without changes to the underlying solver.

3. Methodology

3.1. Overview

At every time step the framework builds two independent OpenSees finite element models, one for the bridge and one for the vehicle. The bridge is a standard Euler–Bernoulli beam discretised with `elasticBeamColumn` elements; the vehicle uses lumped masses together with `zeroLength` spring-dashpot elements for the suspension and tyre assemblies. The two models are then coupled iteratively in five steps: (i) the bridge deflection at every axle is interpolated and added to the road roughness to obtain the vehicle input; (ii) the vehicle is

solved for one time step under that displacement excitation; (iii) the axle reactions are mapped back onto the bridge nodes; (iv) the bridge is solved for one time step under the updated nodal forces; and (v) the bridge displacement field is checked for convergence. The procedure is sketched in Figs. 3 and 4; Fig. 1 shows the underlying physical setup.

The coupling layer interacts with the bridge model through a small interface: it needs (i) the coordinates of the deck nodes along the vehicle path, (ii) the vertical displacement and velocity of those nodes after each step, and (iii) the ability to apply vertical nodal forces to them. Everything else about the bridge, including the element type, the supports, any substructure, and any additional load pattern, is internal to the bridge construction routine and is invisible to the coupling. The same holds for the vehicle: the coupling prescribes the motion of the contact nodes and reads their reactions, and the topology above the contact nodes is free. This separation is what allows the extensions discussed in Section 6.3 without changes to the algorithm.

3.2. Bridge finite element model

The bridge is modelled as a two-dimensional Euler–Bernoulli beam in a 2D frame formulation, using OpenSees `elasticBeamColumn` elements with three degrees of freedom per node (two translations and one rotation). The beam is discretised into N_e elements of uniform length $\Delta x = L/N_e$, giving $N_n = N_e + 1$ nodes. Lumped mass is assigned by tributary length: interior nodes receive $\bar{m}\Delta x$, and the two end nodes receive $\bar{m}\Delta x/2$, where $\bar{m}$ is the mass per unit length. The first support is a pin (fixed in x and y, free in rotation), and the remaining supports are rollers (fixed in y only). Multi-span continuous bridges are obtained by specifying the locations of the intermediate supports. The straight beam on point supports is the configuration used in this paper, but it is not a restriction of the method: the bridge construction routine is an ordinary OpenSees model definition, so bearings, piers, pile caps, and foundation springs can be added with linear OpenSees elements (`zeroLength` springs and dashpots, `elasticBeamColumn` piers, and lumped-parameter soil models as in Bucinskas and Andersen (2020), provided the deck nodes along the vehicle path remain the interface with the coupling layer. Section 6.3 demonstrates this with a deck on flexible vertical supports. History-dependent bearings, yielding piers, and nonlinear soil require material-state preservation and are outside the released implementation (Section 6.4).

Rayleigh damping uses the mass- and committed-stiffness-proportional coefficients obtained from the target damping ratio ζ and the first two natural frequencies:

$$\alpha_M = \zeta \frac{2\omega_1\omega_2}{\omega_1 + \omega_2}, \qquad \beta_K = \frac{2\zeta}{\omega_1 + \omega_2} \tag{9}$$

where ω_1 and ω_2 are the first two circular natural frequencies from the eigenvalue analysis of the bridge model. Time integration uses the Newmark method (Newmark, 1959) with $\gamma = 0.5$ and $\beta = 0.25$ (constant average acceleration), which is unconditionally stable (Chopra, 2017).

At every time step the bridge model is rebuilt in OpenSees after a `wipe` command. The previous-step initial conditions are imposed with `setNodeDisp`, `setNodeVel`, and `setNodeAccel`, the current nodal force time series is applied, and one transient step is solved. Rebuilding at every step avoids the need to maintain persistent state inside OpenSees and removes any risk of conflict between the vehicle and bridge model definitions during the iterative coupling.

3.3. Vehicle finite element models

The framework implements the five vehicle model types described in Section 2 (Fig. 2). The vehicle models are built in OpenSees with lumped masses at the DOF nodes and with `zeroLength` or `twoNodeLink` elements that use `Elastic` materials for the springs and dashpots. The axle (wheel) nodes are constrained as fixed supports. At every time step, both the displacement and the velocity at each axle are imposed through OpenSees' `MultipleSupport` pattern with `imposedMotion`. The displacement time series is the sum of the interpolated bridge deflection and the road roughness at the axle location, and the velocity follows the trajectory derivative described in Section 3.4. Both histories are supplied explicitly to the imposed-motion pattern. The axle reactions are obtained via OpenSees' `nodeReaction` with the `-dynamic` and `-rayleigh` flags, and they represent the total dynamic contact force between the vehicle and the bridge. The sign and magnitude of this reaction were verified against the analytical contact-force expression $F_c = k(y - u_c) + c(\dot{y} - \dot{u}_c)$ on a static imposed-settlement test and against the benchmark references of Section 4; the total force transmitted to the bridge equals the static axle load plus this dynamic reaction throughout the analysis.

For the single-axle models (simple and composite), a 1D OpenSees model (`ndm = 1`) is used: the axle node is fixed, and the body and axle masses are connected by `zeroLength` spring-dashpot elements. For the half-car models with body pitch (comp2 and comp3), a 2D frame formulation (`ndm = 2`, `ndf = 3`) is needed to represent the rotational DOF. The body centre of gravity is a node that carries the body mass and the pitch moment of inertia and is connected to the suspension attachment points above each axle through high-stiffness penalty links (`twoNodeLink` elements with stiffness $\sim 10^6 \times k_s$). The penalty links enforce near-rigid-body kinematics between the CG node and the suspension tops, so that the body bounce and the pitch reach the axle positions through the suspension springs without introducing extra flexible modes. Table 11 in the Appendix gives the complete node and element connectivity for every vehicle model type.

Two features of the vehicle models deserve emphasis. First, the contact (wheel) nodes are kinematically driven: their vertical displacement and velocity are prescribed, so they carry no mass and no dynamic degree of freedom, and the contact force is simply the support reaction at the prescribed node. This is why the wheel markers in Fig. 2 carry no DOF label; in the composite models the unsprung (axle) mass is a separate node above the contact node. Second, because the vehicle is an ordinary OpenSees model, richer topologies are added by defining more nodes and elements above the contact nodes. A multi-body railway vehicle (car body with bounce and pitch, two bogies with bounce and pitch, four wheelsets) follows the same template as the composite half-car with additional intermediate rigid bodies and suspension layers, and additional contact nodes can be accommodated after extending the vehicle builder, state allocation, and configuration parser. A track layer (rails on discrete pads and sleepers) belongs to the bridge side of the interface and is added in the bridge construction routine, the rail nodes then being the nodes seen by the coupling. Nonlinear contact laws, such as Hertzian wheel-rail contact (Antolín et al., 2013), require a unilateral contact formulation with separation and re-contact, a compatible nonlinear solve, and preservation of any history-dependent state. Changing only the tyre material or solver is insufficient. None of these extensions is exercised in the present paper; they are listed to make clear which parts of the framework they would touch.

A single static analysis is run at the start of the simulation to obtain the static axle forces under gravity. These static forces are the baseline moving load applied to the bridge in the absence of any dynamic effects.

3.4. Force mapping

The axle positions in general do not coincide with bridge nodes, so the vehicle contact forces have to be mapped onto the nearest bridge nodes. Linear shape function interpolation is used: for an axle at position x_a inside element $[x_i, x_{i+1}]$ of length ℓ, the force F_a is distributed to the two element nodes as

$$F_i = \left(1 - \frac{x_a - x_i}{\ell}\right) F_a, \qquad F_{i+1} = \frac{x_a - x_i}{\ell} F_a \tag{10}$$

where x_i and x_{i+1} are the coordinates of the element end nodes. This two-node linear transfer is an approximation to the cubic Hermite beam

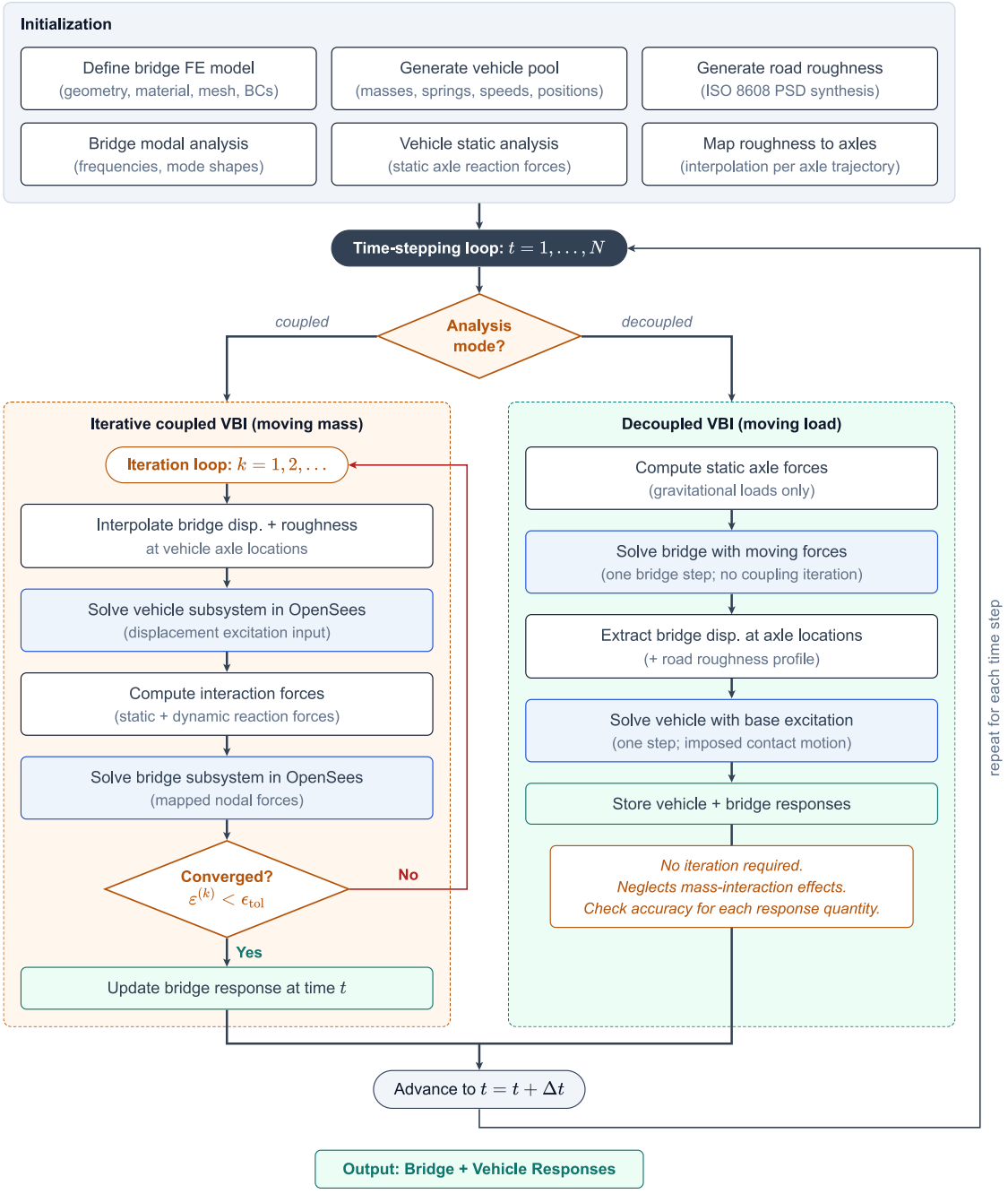

Fig. 3. Framework flowchart. Phase 1 (initialisation): the bridge model, the vehicle pool, and the road roughness profile are built, and the static axle loads are computed. Phase 2 (time stepping): at each step the analysis follows one of two branches. In the coupled branch (left), the bridge deflection and roughness at each axle define the vehicle input, the vehicle is solved, the axle reactions are mapped to the bridge, the bridge is re-solved, and the loop repeats until the displacement residual of Eq. (6) falls below the tolerance. In the decoupled branch (right), the bridge is solved once per time step under the static moving loads and the vehicle is then base-excited by the resulting contact motion. Both branches store the bridge and vehicle responses before advancing to the next step.

interpolation; it preserves both the total force and its first moment. When an axle is outside the bridge span (before it enters or after it exits), it does not contribute to the bridge loading.

The same interpolation order is used in the opposite direction: the bridge motion is transferred to the vehicle by linear interpolation of the nodal displacement and nodal velocity fields at the axle position. The vehicle trajectory enters through the sampled position history $x_a(t)$ of each axle. For a prescribed non-negative speed profile, $x_a(t) = x_{a,0} + \int_0^t v(\tau)\,\mathrm{d}\tau$; no constant-speed assumption is required by the coupling iteration. The contact-point velocity is the derivative along the moving path,

$$\dot{u}_c(t) = \frac{\partial w}{\partial t}(x_a, t) + v(t)\frac{\partial w}{\partial x}(x_a, t) + \frac{\mathrm{d}r(x_a(t))}{\mathrm{d}t}.$$

The first term uses the interpolated nodal velocities, the second uses the slope of the same piecewise-linear displacement interpolant, and the roughness term is differentiated along each axle's own trajectory. Using each axle's trajectory matters for variable speed: shifting the leading axle's roughness-velocity history would assign an earlier speed to a trailing axle. The convective term contributes to the contact force when the contact element includes damping. For the undamped contact

elements used in the numerical benchmarks and the two quarter-cars, the contact-force law contains no velocity-dependent term.

The slope of this interpolant is discontinuous at beam nodes. Section 4.5 checks mesh sensitivity of benchmark peak deflection; it does not bound node-crossing effects in high-frequency acceleration or contact-force responses.

3.5. Iterative coupling algorithm

The complete iterative coupling procedure at time step t_{n+1} is formalised in Algorithm 1.

Algorithm 1 Iterative Coupled VBI Analysis at Time Step t_{n+1}

Require: Bridge state at t_n: $\{\mathbf{w}_n, \dot{\mathbf{w}}_n, \ddot{\mathbf{w}}_n\}$; Vehicle state at t_n; Road roughness $r(x)$; Axle trajectories $x_a(t)$; External nodal force history $\mathbf{F}_{\text{ext}}(t)$
Ensure: Updated bridge and vehicle states at t_{n+1}
Initialise $\mathbf{w}_{n+1}^{(0)}$ from the precomputed external-load-only bridge response
Set iteration counter $k \leftarrow 0$
repeat
  $k \leftarrow k + 1$
  for each vehicle v **do**
    for each axle i of vehicle v **do**
      Compute axle position: $x_{a,i} = x_{\text{rear}}(t_{n+1}) + d_i$
      Interpolate bridge displacement and velocity at $x_{a,i}$
      Compute axle displacement: $u_i = w_b(x_{a,i}) + r(x_{a,i})$
      Compute axle velocity: $\dot{u}_i = \partial_t w_b(x_{a,i}, t) + v_i(t)\partial_x w_b(x_{a,i}, t) + \dot{r}(x_{a,i}(t))$
    end for
    Solve vehicle FE model with imposed displacement $\{u_i\}$ and velocity $\{\dot{u}_i\}$
    Extract axle reaction forces $\{F_{a,i}\}$ via `nodeReaction(-dynamic, -rayleigh)`
  end for
  Initialise nodal force vector: $\mathbf{F}_{\text{inter}} \leftarrow \mathbf{0}$
  for each vehicle v, each axle i **do**
    $F_{\text{total},i} \leftarrow F_{\text{static},i} + F_{a,i}^{\text{dynamic}}$
    if $F_{\text{total},i} > 0$ **then** ▷ Compressive contact only; uplift gives zero force
      Map $F_{\text{total},i}$ to bridge nodes using Eq. (10)
    end if
  end for
  Add the external nodal force history (background traffic in this paper): $\mathbf{F}_n \leftarrow \mathbf{F}_{\text{ext}}(t_{n+1}) + \mathbf{F}_{\text{inter}}$
  Solve bridge FE model in OpenSees with nodal forces $\mathbf{F}_n$
  Extract updated bridge response $\mathbf{w}_{n+1}^{(k)}$
  Compute convergence residual $\varepsilon^{(k)}$ using Eq. (6)
until $\varepsilon^{(k)} < \epsilon_{\text{tol}}$
Store converged bridge and vehicle states at t_{n+1}

The initial iterate is taken from a precomputed bridge history under external loads alone, starting from the analysis initial conditions. Each trial transient solve then starts from the previous converged coupled state; the precomputed history supplies an initial guess rather than the committed state for integration. For all validation studies in this paper, the convergence tolerance on the bridge displacement residual $\varepsilon^{(k)}$ (Eq. (6)) is set to $\epsilon_{\text{tol}} = 10^{-12}$, which makes the benchmark comparisons independent of the iteration error; for engineering accuracy in practice, values between 10^{-4} and 10^{-6} are usually sufficient (the tolerance study in Section 4.5 quantifies this). With this initialisation the algorithm converged in at most five iterations per time step for the benchmark configurations, in at most seven for the heavy quarter-car cases, and in at most 29 for the stiff single-DOF frequency grid. A 100-iteration failure cap and a non-finite-residual check prevent an unsuccessful solve from being reported as converged.

External excitation. The array named `random_traffic_force_time` in the implementation is an additive vertical nodal-force history. It can also hold prescribed wind forces or effective seismic forces, provided sign and coordinate conventions are consistent. Motion-dependent loads require a callback inside the iteration. Section 6.3 specifies the additional support-motion and vehicle-input changes; these extensions have not been validated in this paper.

3.6. Simplified decoupled approach

When an approximation of the dynamic feedback is acceptable, the framework offers a decoupled (non-iterative) analysis mode. The procedure is summarised in Algorithm 2.

Algorithm 2 Decoupled VBI Analysis (Moving Load + Base Excitation)

Require: Bridge and vehicle properties; roughness $r(x)$; axle trajectories $x_a(t)$; external vertical force history
Ensure: Bridge and vehicle response histories
Compute static axle forces $\{F_{\text{static},i}\}$
for each time step t_{n+1} **do**
  Map static axle forces at $x_{a,i}(t_{n+1})$ to bridge nodes
  Add the prescribed external nodal forces
  Rebuild and advance the bridge once from its state at t_n
  for each vehicle **do**
    Interpolate contact displacement and trajectory velocity (Section 3.4)
    Rebuild and advance the vehicle once under the imposed contact motion
  end for
  Store bridge and vehicle states; do not feed dynamic axle forces back to the bridge
end for

The decoupled approach applies constant axle weights to the bridge and uses the resulting bridge motion to excite the vehicle. The released implementation advances and rebuilds each subsystem once per time step, without a coupling iteration. For prescribed force histories the bridge could instead be advanced for the entire history in one persistent model, but that is a separate bridge-only timing baseline in Section 6.1. The acceptability of the decoupled approximation depends on the requested response, vehicle and bridge frequencies and damping, mass ratio, speed, and excitation.

3.7. Road roughness generation

Roughness profiles are generated from the ISO 8608 spectral model of Eqs. (7) and (8) over the spatial frequency band $[n_l, n_u]$ with increment Δn. The profile covers the entire analysis window, including approach roads before and after the bridge, so that the vehicle suspension is already excited by road roughness when the vehicle enters the bridge.

The roughness input to each axle includes the spatial lag between axles. For a vehicle with axles at local coordinates $\{d_0, d_1, \ldots, d_{N_a-1}\}$ measured from the rear axle, and with rear-axle position history $x_{\text{rear}}(t)$, the roughness seen by axle i at time t is $r(x_{\text{rear}}(t)+d_i)$. The corresponding velocity input follows from the chain rule, $\dot{r} = v\, r'(x)$, evaluated on the sampled profile. The optional moving-average filter spans 0.25 m (five samples of the 0.05 m spatial mesh), which is of the order of a tyre contact patch. It is a numerical smoothing choice rather than a validated tyre-enveloping model; its effect on the synthesised spectrum is quantified in Section 4. Because the model is planar, a single-track profile is used: left and right wheels are not distinguished, and the comp1 variant with independent half-vehicles receives the same profile on both tracks.

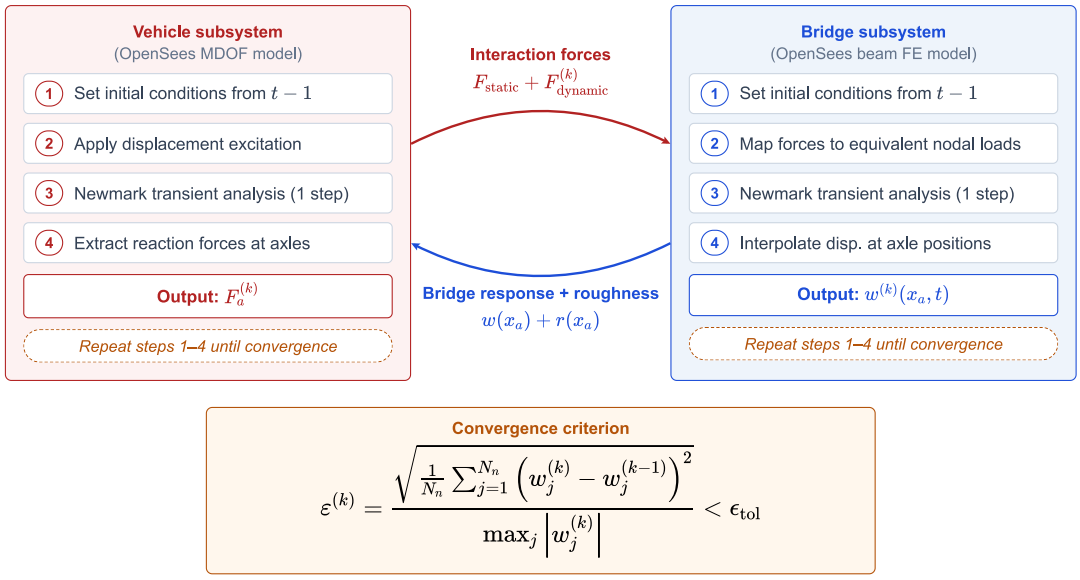

Fig. 4. Iterative partitioned coupling at a single time step. The vehicle subsystem (left) receives the imposed axle displacement and velocity, is advanced by one Newmark step, and returns the dynamic axle reactions. The bridge subsystem (right) receives the mapped nodal forces (static axle loads plus dynamic reactions plus background traffic), is advanced by one step from the previous converged state, and returns the updated deflection field. The exchange repeats within the time step until the normalised displacement residual (bottom) meets the tolerance ϵ_{tol}.

4. Validation

This section numerically verifies the implementation on three benchmark configurations from the VBI literature, spanning the framework's vehicle model classes from a single-axle sprung mass to a full two-axle composite half-car, against references that share no code or spatial discretisation with it.

4.1. Reference solutions and error metrics

For Benchmarks 1 and 2, the framework is compared with the published finite element results of Yang et al. (2004a, 2019) for the same configurations. For Benchmark 3, it is compared with a reference solution of the published configuration that is obtained independently of the framework: it uses a different spatial representation of the bridge, a different time integrator, and a different treatment of the vehicle–bridge coupling, and shares no source code with the framework. Agreement therefore cannot be inherited from shared numerics. This reference solver is released together with the framework so that every comparison in this section can be regenerated; its curves are labelled "Independent modal reference". Numerical references were chosen deliberately: they allow every input of the benchmark to be matched exactly, so that the comparison isolates the coupling algorithm and its implementation from modelling choices. They do not test the modelling assumptions themselves (planar beam, point contact, linear suspension), which only a field or laboratory dataset with fully documented vehicle and bridge parameters can do; this gap is discussed in Section 6.4.

Agreement is quantified by three complementary metrics computed on the crossing window: the coefficient of determination

$$R^2 = 1 - \frac{\sum_n \left(y_r(t_n) - y_f(t_n)\right)^2}{\sum_n \left(y_r(t_n) - \bar{y}_r\right)^2}, \tag{11}$$

where y_f and y_r are the framework and reference histories and $\bar{y}_r$ is the reference mean; the root-mean-square error normalised by the reference range (NRMSE); and the relative error of the peak absolute response. R^2 measures waveform agreement, NRMSE the average amplitude error, and the peak error the quantity that governs design checks. All coupled analyses use the tolerance $\epsilon_{\text{tol}} = 10^{-12}$.

Table 2
Bridge and vehicle parameters for Benchmark 1 (Yang et al., 2004a).

Parameter	Symbol	Value	Unit
Bridge			
Span length	L	25	m
Elastic modulus	E	2.75×10^{10}	Pa
Second moment of area	I	0.12	m^4
Cross-sectional area	A	2.0	m^2
Mass per unit length	$\bar{m}$	4800	kg/m
Damping ratio	ζ	0	–
Vehicle			
Sprung mass	m_v	1200	kg
Suspension stiffness	k_v	5.0×10^5	N/m
Suspension damping	c_v	0	N s/m
Speed	v	10	m/s

4.2. Benchmark 1: Single-axle sprung-mass vehicle (Yang et al., 2004a)

The first benchmark reproduces the configuration of Yang et al. (2004a), who analysed a quarter-car spring-mass vehicle crossing a simply supported beam. The vehicle and bridge parameters are listed in Table 2.

Fig. 5 compares the framework, using 500 beam elements and a 1000 Hz sampling rate, with the published results of Yang et al. (2004a) for this sprung-mass configuration. The two solutions are indistinguishable: $R^2 = 1.0000$ for both the bridge midspan and the vehicle body displacement, with NRMSE of 0.11 % and 0.12 % and peak errors of −0.02 % (Table 5). The vehicle mass (1200 kg) is small compared with the bridge mass (4800 kg/m × 25 m = 120,000 kg), giving a mass ratio $\mu = 1$ %. The bridge fundamental frequency (2.08 Hz) and the vehicle frequency (3.25 Hz) are well separated, so the response is dominated by the first beam mode.

4.3. Benchmark 2: Half-car vehicle with pitch (Yang et al., 2019)

The second benchmark increases the vehicle model complexity to the asymmetric half-car with body pitch of Yang et al. (2019). The vehicle and bridge parameters are listed in Table 3.

Fig. 6 compares the framework (600 beam elements, 500 Hz sampling) with the published results of Yang et al. (2019). The vehicle mass

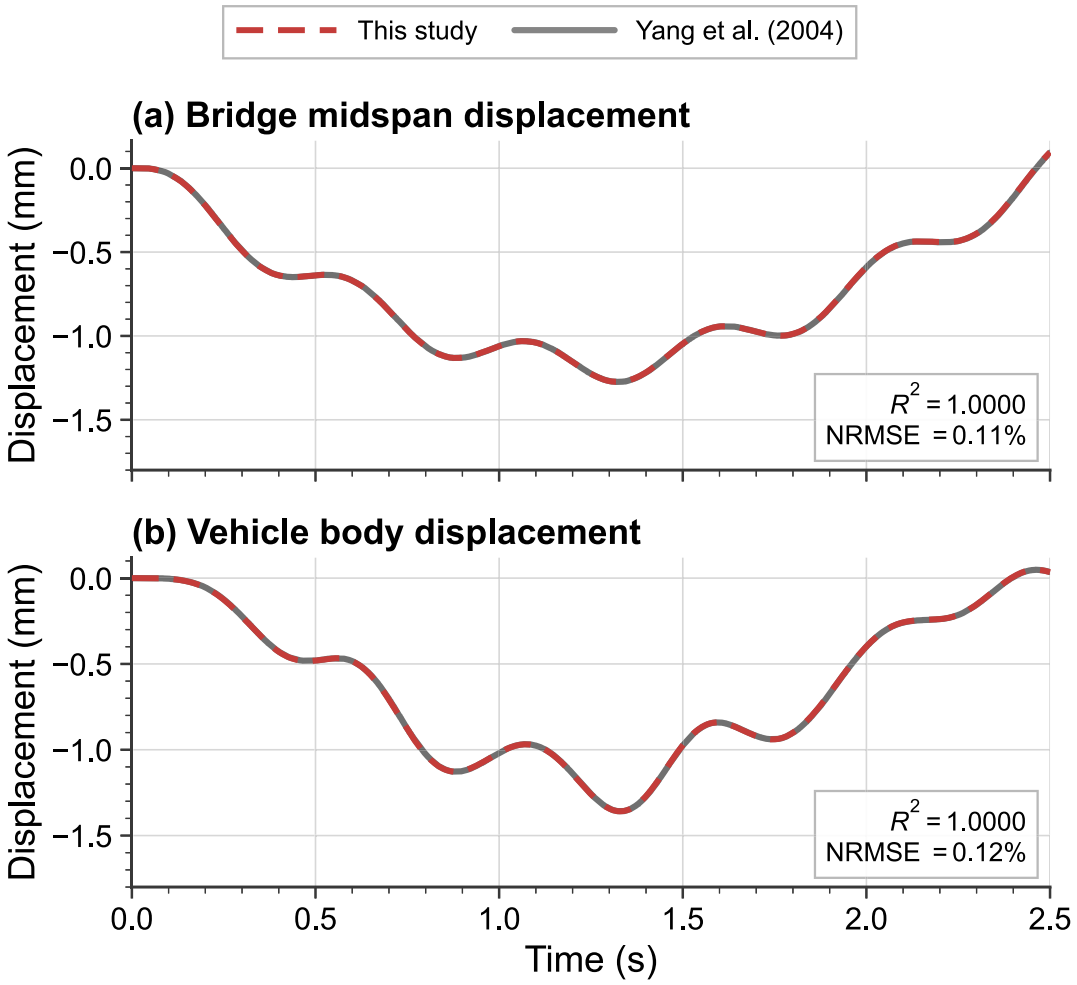

Fig. 5. Benchmark 1 (sprung-mass vehicle of Yang et al. (2004a) on a 25 m simply supported beam): framework (red dashed) against the published results of Yang et al. (solid grey). (a) Bridge midspan displacement; (b) vehicle body displacement.

Table 3
Bridge and vehicle parameters for Benchmark 2 (Yang et al., 2019).

Parameter	Symbol	Value	Unit
Bridge			
Span length	L	30	m
Flexural rigidity	EI	5.5×10^9	N m^2
Mass per unit length	$\bar{m}$	2000	kg/m
Damping ratio	ζ	0	–
Vehicle			
Body mass	m_v	2500	kg
Pitch moment of inertia	J_v	2300	kg m^2
Front suspension stiffness	k_f	2.3×10^5	N/m
Rear suspension stiffness	k_r	1.8×10^5	N/m
Front suspension damping	c_f	0	N s/m
Rear suspension damping	c_r	0	N s/m
Axle spacing	d	3	m
CG to front axle	d_1	1.7	m
CG to rear axle	d_2	1.3	m
Speed	v	10	m/s

(2500 kg) and the bridge mass (2000 kg/m × 30 m = 60,000 kg) give a mass ratio of about 4.2 %, the largest among the three benchmarks. The peak midspan displacement is about 2.6 mm and occurs when the vehicle is near mid-span; the response is multi-modal because of the asymmetric half-car loading. The bridge midspan displacement and the vehicle body displacement agree with the published histories at R^2 = 1.0000 (NRMSE 0.11 %), and the pitch rotation agrees at R^2 = 0.9999 (NRMSE 0.26 %); the peak errors are at most 0.14 % (Table 5).

4.4. Benchmark 3: NuBe vehicle models (Cantero et al., 2024)

The third benchmark uses vehicle and bridge configurations from the NuBe numerical benchmark dataset (Cantero et al., 2024), which provides a standardised set of VBI simulation results obtained with the independent VBI-2D MATLAB solver (Cantero, 2024). The framework is configured with the mean vehicle properties of the NuBe V1 (quarter-car) and V2 (full composite half-car) models, running on the NuBe B27 bridge (27 m span). The bridge and vehicle parameters are listed in Table 4.

The NuBe configurations exercise two further vehicle model types on the same bridge (Fig. 7), both with non-zero suspension damping: the composite quarter-car and the full two-axle composite half-car with independent axle masses. The V1 quarter-car (total mass 9100 kg, mass ratio $\mu \approx 1.7$ %) produces a smooth midspan deflection dominated by the first beam mode; the framework matches the reference solution with $R^2 = 0.9997$ for the bridge and $R^2 = 0.9998$ for the body, with peak errors below 0.07 % (Table 5). The V2 half-car (total mass 12,300 kg, $\mu \approx 2.4$ %) shows a richer response because of the pitching motion and the separate excitation at the two contact points; here the agreement reaches $R^2 = 1.0000$ for both bridge and body with NRMSE below 0.04 %. Adopting these configurations from the openly documented NuBe benchmark dataset (Cantero et al., 2024) also makes the present validation cases directly comparable with an established community reference for drive-by studies.

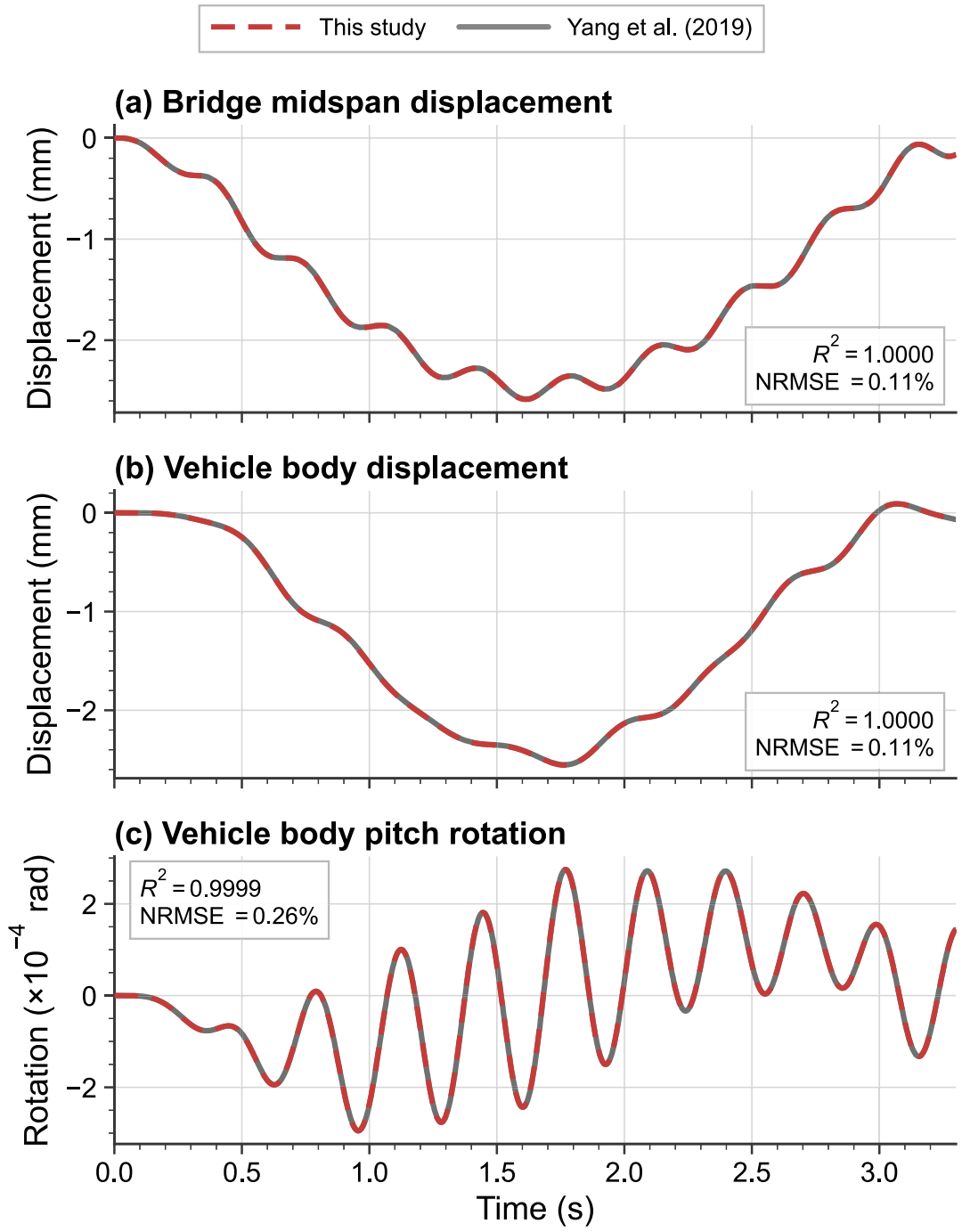

Fig. 6. Benchmark 2 (half-car with pitch of Yang et al. (2019) on a 30 m simply supported beam): framework (red dashed) against the published results of Yang et al. (solid grey). (a) Bridge midspan displacement; (b) vehicle body displacement; (c) vehicle body pitch rotation. In (c), the published rotations are plotted at ten times their printed axis values (labelled $\times 10^{-4}$ rad), i.e., on the $\times 10^{-3}$ scale of the published displacement figures; with the printed label, the pitch would be smaller than the quasi-static deck slope under the vehicle (about 1.3×10^{-4} rad).

4.5. Convergence, discretisation, and sensitivity studies

Iteration behaviour. Table 6 reports the iteration statistics of the coupling loop at $\epsilon_{\text{tol}} = 10^{-12}$ for the three benchmarks and for deliberately demanding configurations from the parametric study of Section 5, in which the heavy truck exceeds the bridge mass by a factor of up to 24. Across all benchmark cases the loop converges in at most 4–5 iterations per step. Even at $\mu \approx 24.5$, the most extreme mass ratio considered anywhere in this paper, the maximum count only rises to 7, and changing the roughness from level R2 to level R3 leaves the statistics unchanged. The iteration count is highest while the vehicle is on the span and drops once it exits. These counts document convergence for the tested linear configurations; they do not establish unconditional convergence of the partitioned scheme. The frequency-ratio map of Section 5.2 extends these statistics to stiff, heavy vehicles: the maximum count grows with both the mass ratio and the frequency ratio. All 56 cases converged without relaxation and below the 100-iteration failure cap; the maximum count is reported in Section 5.2.

Tolerance sensitivity. Re-running Benchmark 2 with ϵ_{tol} relaxed from 10^{-12} to 10^{-6} changes the midspan displacement history by less than

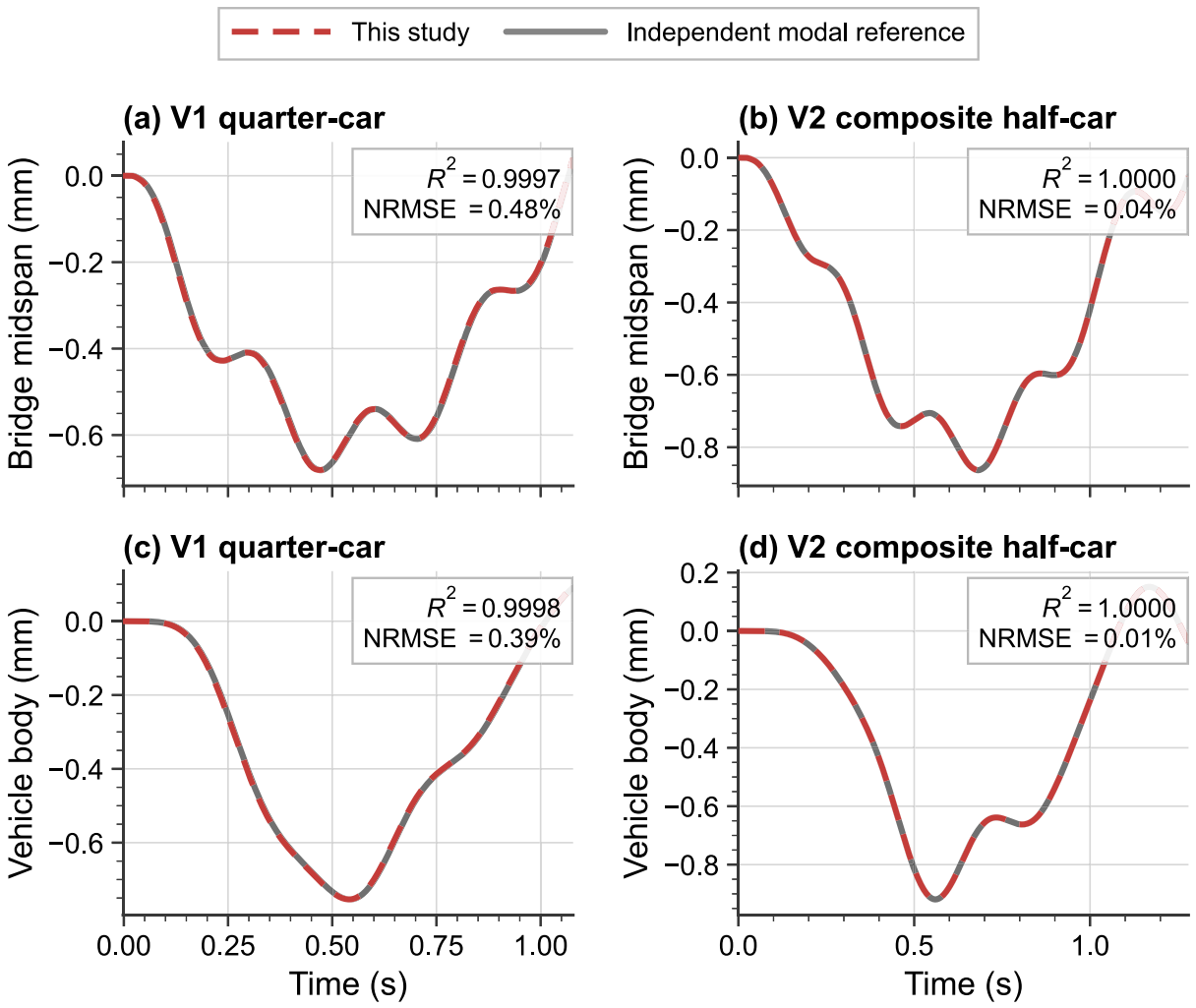

Fig. 7. Benchmark 3: bridge midspan displacement (top) and vehicle body displacement (bottom) for the NuBe V1 (quarter-car, left) and V2 (full composite half-car, right) configurations on the B27 bridge (27 m, smooth road): framework (red dashed) against the independent modal reference (solid grey) for each configuration.

5×10^{-10} of its peak while reducing the mean iteration count from 4.4 to 2.9; even 10^{-4} keeps the maximum relative deviation below 4×10^{-6} at 2.0 iterations per step. The tight tolerance used for the benchmarks is therefore a conservative choice that removes iteration error from the comparisons, not a requirement of the method.

Mesh and time-step convergence. For Benchmark 1, refining the bridge mesh from 50 to 1000 elements changes the peak midspan displacement by less than 0.06 % (1.2734 mm to 1.2738 mm, converged from 250 elements on), and increasing the sampling rate from 250 Hz to 2000 Hz changes it by less than 0.06 % (converged from 500 Hz on). For this deflection metric, changes are small from 250 elements and 500 Hz onward. This check does not establish convergence of acceleration or contact-force histories for every bridge, vehicle, and roughness input.

Penalty-link sensitivity. The half-car models enforce the rigid-body connection between the centre of gravity and the suspension attachment points through penalty links with stiffness $10^6 k_s$ (Section 3.3). Scaling this penalty by factors of 10^{-2} to 10^2, i.e., across four orders of magnitude ($10^4 k_s$ to $10^8 k_s$), changes the peak bridge displacement, body displacement, and pitch rotation of Benchmark 2 by less than 0.004 % each. Mean iteration counts range from 4.43 to 4.44 at the fixed 0.005 s time step. These results establish low sensitivity of the reported peaks in this case, not a general stability guarantee for stiff penalty modes or nonlinear contact.

Roughness spectrum verification. Fig. 8 compares the power spectral density of generated levels R1, R2, and R3 profiles, estimated with Welch's method over a 2 km profile, with the ISO 8608 target spectra. Before smoothing, the synthesised profiles track the target within about 10 % in the geometric mean over 0.02–5 cycles/m for every level. The optional 0.25 m moving-average filter leaves wavelengths longer than 1 m little affected (about 13 % PSD reduction in the geometric mean below 1 cycle/m) and progressively suppresses shorter wavelengths; this filter has not been calibrated as a tyre-enveloping model; the profiles are sampled at 0.05 m so that all wavelengths longer than 1 m have at least 20 spatial samples. The 0.1 m lower wavelength limit is at the spatial Nyquist limit; at 30 m/s it corresponds to 300 Hz, above the 250 Hz temporal Nyquist frequency of the 500 Hz simulations. The filter attenuates but does not strictly remove those components. High-frequency accelerations and contact forces therefore require finer spatial and temporal sampling.

5. Parametric study: Coupled vs. decoupled analysis

This section compares coupled and decoupled responses over bridge, vehicle, and excitation parameters. The total-mass ratio $\mu = m_v/(\bar{m}L)$

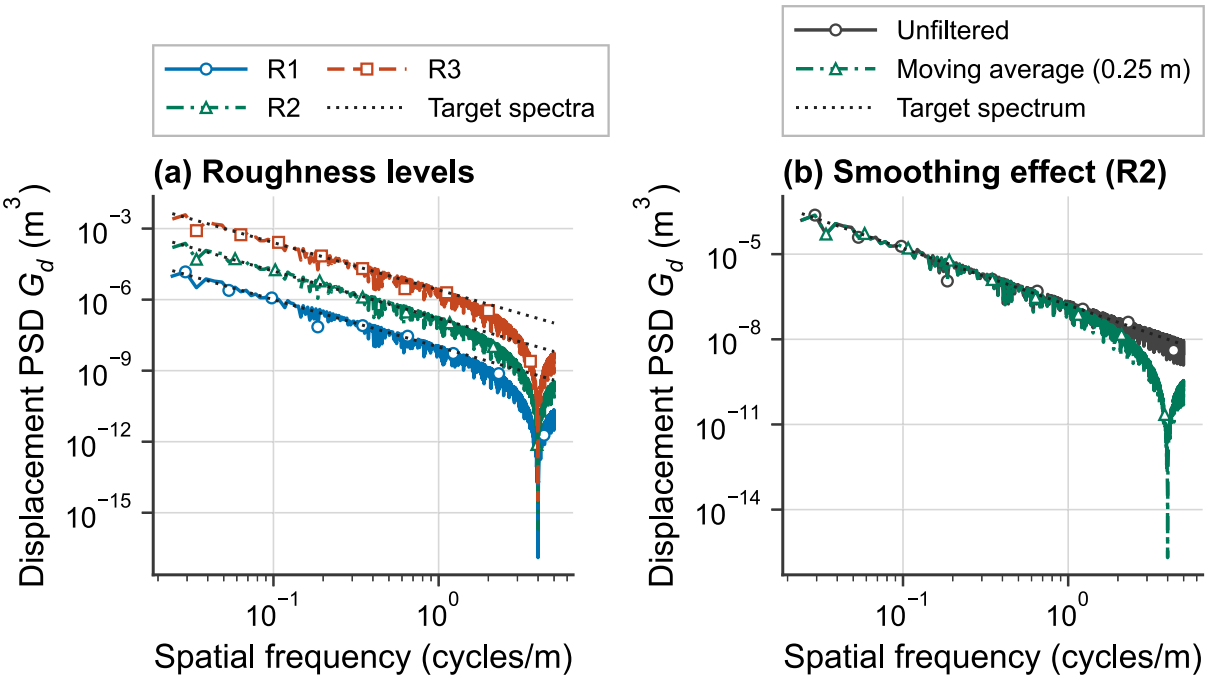

Fig. 8. Verification of the roughness generator against the ISO 8608 spectral targets. Left: PSD of generated levels R1, R2, and R3 profiles, distinguished by line styles and circle, triangle, and square markers, respectively, versus the target spectra (black dotted). Right: effect of the optional 0.25 m moving-average filter on a level R2 profile; wavelengths longer than 1 m are little affected.

Table 4
Bridge and vehicle parameters for Benchmark 3, using mean values from the NuBe dataset (Cantero et al., 2024).

Parameter	Symbol	Value	Unit
Bridge (B27)			
Span length	L	27	m
Young's modulus	E	3.5×10^{10}	Pa
Second moment of area	I	1.7055	m^4
Mass per unit length	$\bar{m}$	19,372	kg/m
Damping ratio	ζ	0	–
First natural frequency	f_1	3.7824	Hz
Vehicle V1 (quarter-car)			
Body mass	m_B	8000	kg
Axle mass	m_G	1100	kg
Suspension stiffness	k_S	2.0×10^6	N/m
Suspension damping	c_S	4.0×10^4	N s/m
Tyre stiffness	k_T	3.5×10^6	N/m
Speed	v	25	m/s
Vehicle V2 (half-car)			
Body mass	m_{B1}	10,500	kg
Axle mass (each)	m_G	900	kg
Body moment of inertia	I_{B1}	50,000	kg m^2
Suspension stiffness (each)	k_S	6.0×10^6	N/m
Suspension damping (each)	c_S	1.0×10^4	N s/m
Tyre stiffness (each)	k_T	1.75×10^6	N/m
Axle spacing	d	5.0	m
Speed	v	25	m/s

Table 5
Validation metrics for the three benchmarks: framework versus the reference for each configuration (for Benchmarks 1 and 2, the published results of Yang et al. (2004a, 2019), computed on the crossing window. NRMSE is normalised by the reference range.

Benchmark	Response	R^2	NRMSE (%)	Peak error (%)
B1	Bridge midspan	1.0000	0.11	−0.02
B1	Vehicle body	1.0000	0.12	−0.02
B2	Bridge midspan	1.0000	0.11	+0.11
B2	Vehicle body	1.0000	0.11	+0.13
B2	Pitch rotation	0.9999	0.26	+0.14
B3-V1	Bridge midspan	0.9997	0.48	−0.066
B3-V1	Vehicle body	0.9998	0.39	−0.005
B3-V2	Bridge midspan	1.0000	0.039	−0.046
B3-V2	Vehicle body	1.0000	0.009	+0.006

Table 6
Iteration statistics of the coupling loop at $\epsilon_{\text{tol}} = 10^{-12}$. The demanding cases use the Eshkevari bridges of Table 7 with ISO 8608 roughness.

Case	μ	Mean iterations	Max
B1, sprung mass	0.010	3.97	4
B2, half-car with pitch	0.042	3.97	4
B3-V1, quarter-car	0.017	3.98	4
B3-V2, composite half-car	0.024	3.97	4
15 m bridge, heavy truck, level R2	24.5	3.78	7
15 m bridge, heavy truck, level R3	24.5	3.78	7
30 m bridge, heavy truck, level R2	5.0	4.14	6
30 m bridge, commercial vehicle, level R2	0.15	2.95	4

and the frequency ratio $r = f_v/f_1$ are reported together; neither ratio alone guarantees an accurate approximation. The study includes four simply supported numerical bridge configurations, two quarter-cars, six speeds, three stated roughness levels, and four background-load levels. The configurations follow Sadeghi Eshkevari et al. (2020b); they are used to probe a wide interaction range, not as representative full-scale bridge cross-sections. The controlled single-DOF sweep then varies mass and frequency ratios independently at fixed speed and damping.

Table 7 lists the bridge configurations, which follow the medium- to long-span set of Sadeghi Eshkevari et al. (2020b). The second moment of area I is computed from the box cross-section dimensions, and the mass per unit length $\bar{m}$ is calibrated to match the fundamental frequency of each span using the Euler–Bernoulli formula $f_1 = (\pi/2L^2)\sqrt{EI/\bar{m}}$ with $E = 27.5$ GPa. The resulting $\bar{m}$ values are low for the section sizes, so the set spans an unusually wide range of mass ratios; it is used here because it is documented and because it probes the strong-interaction regime. Two quarter-car vehicles from the same source are used: the commercial vehicle (total mass 535.9 kg) and the heavy truck (total mass 18,000 kg). The "heavy truck" is a single-axle-group idealisation in which the full vehicle mass is lumped into one

Table 7
Bridge configurations for the parametric study, adapted from Eshkevari et al. The second moment of area I is computed from the box cross-section dimensions; the mass per unit length $\bar{m}$ is calibrated to match the target fundamental frequency. The mass ratios $\mu = m_v/(\bar{m}L)$ are given for the commercial vehicle (535.9 kg) and the heavy truck (18,000 kg).

Span (m)	Depth (m)	Width (m)	t_f (m)	t_w (m)	I (m^4)	$\bar{m}$ (kg/m)	f_1 (Hz)	μ_{comm}	μ_{heavy}
15	0.60	0.30	0.04	0.02	0.0024	49	8.03	0.7303	24.530
30	1.10	0.50	0.05	0.03	0.0188	119	3.63	0.1495	5.022
50	1.60	1.30	0.10	0.05	0.1693	437	2.05	0.0245	0.823
100	2.40	2.00	0.15	0.10	0.9148	1104	0.75	0.0049	0.163

Table 8
Dynamic properties of the two parametric-study vehicles (2-DOF quarter-cars) and their vehicle-to-bridge frequency ratios $r = f_v/f_1$ on the four bridges of Table 7. f_v is the undamped natural frequency of the body-bounce or axle-hop mode; ζ_s is the suspension damping ratio referred to the sprung mass.

Vehicle	Mode	f_v (Hz)	r (15 m)	r (30 m)	r (50 m)	r (100 m)
Commercial (535.9 kg, $\zeta_s = 3.80$)	Bounce	0.120	0.015	0.033	0.059	0.160
	Hop	1.10	0.137	0.303	0.536	1.47
Heavy truck (18,000 kg, $\zeta_s = 0.060$)	Bounce	0.690	0.086	0.190	0.337	0.920
	Hop	8.83	1.10	2.43	4.31	11.8

sprung-mass assembly, following the source study; it is intended to bound the strong-interaction regime rather than to represent the axle-by-axle load pattern of a real truck, for which the two-axle models of Section 2 are available. Table 8 summarises the dynamic properties of the two vehicles. The commercial vehicle has a very soft and heavily damped suspension ($f_{\text{bounce}} = 0.12$ Hz, suspension damping ratio $\zeta_s \approx 3.8$), so its frequency ratio to every bridge in the set is far below unity; the heavy truck has $f_{\text{bounce}} = 0.69$ Hz and $f_{\text{hop}} = 8.8$ Hz, so its bounce mode approaches the fundamental frequency of the 100 m bridge ($r = 0.92$) and its hop mode approaches that of the 15 m bridge ($r = 1.10$). These ratios are used in Sections 5.1 and 5.2. Unless stated otherwise, all analyses use level R2 roughness based on the ISO 8608 spectrum ($G_d(n_0) = 16\times10^{-6}$ m^3; Table 1), 0.3 % Rayleigh damping, and a constant vehicle speed of 10 m/s. The roughness frequency increment is set to $\Delta n = \min(0.01, 1/(2L))$ cycles/m, so that the period of the generated profile is at least twice the bridge span and no artificial periodicity is introduced for the longer spans.

5.1. Effect of bridge span length

The first investigation varies the bridge span from 15 m to 100 m with the vehicle, roughness, and speed parameters fixed. Both vehicle types are tested on each bridge so that the effects of span length and of vehicle mass can be captured together.

The results show a clear separation between the two vehicle classes. For the commercial vehicle ($m_v \approx 536$ kg), the coupled and decoupled midspan-displacement histories are visually indistinguishable at every span (Fig. 9), and the coefficient of determination R^2 between them stays above 0.999 across all four spans, confirming that a vehicle of this mass has a negligible inertial effect on any of the bridges tested (Fig. 11). For the heavy truck ($m_v \approx 18{,}000$ kg), the two histories diverge visibly (Fig. 10) and the agreement is markedly worse: at the 15 m span ($\mu \approx 24.5$, where the truck outweighs the bridge) R^2 drops well below unity, and even at the 100 m span ($\mu \approx 0.16$) it remains noticeably below the commercial-vehicle value. The vehicle body acceleration R^2 (Fig. 12) follows the same qualitative pattern with an even larger gap between the two vehicles, because the interaction effects are amplified by the suspension dynamics.

The heavy truck's body-acceleration R^2 becomes strongly negative on the 100 m bridge, despite the small mass ratio $\mu \simeq 0.163$. Its undamped bounce frequency is 0.69 Hz and the bridge frequency is 0.75 Hz ($r = 0.92$; Table 8), suggesting a frequency-tuning contribution to the discrepancy (Sadeghi Eshkevari et al., 2020b; Stoura and Dimitrakopoulos, 2020a). A negative R^2 means that the squared prediction error exceeds the variance of the coupled signal; it is not evidence of agreement when the response is small. Both normalised and absolute errors are needed to assess usefulness. The commercial vehicle has a much lower bounce-frequency ratio and a large suspension damping coefficient. Its isolated-suspension ratio $\zeta_s = 3.80$ is not a damping ratio for every mode of the coupled two-DOF vehicle. The bounce/hop ratios, damping, mass split, roughness, and speed must all be considered when interpreting the class difference. In particular, the truck's bounce ratio is only 0.086 on the 15 m bridge, so its poor agreement there cannot be attributed to bounce tuning alone.

5.2. Joint effect of mass ratio and frequency ratio

To separate the two parameters, the 30 m bridge of Table 7 ($f_1 = 3.64$ Hz from the finite element eigenvalue analysis, total mass 3570 kg) is crossed at 10 m/s on a smooth road by a single-axle sprung-mass vehicle whose mass and stiffness are set so that the mass ratio $\mu = m_v/(\bar{m}L)$ and the frequency ratio $r = f_v/f_1 = \sqrt{k_v/m_v}/\omega_1$ take prescribed values: $\mu \in \{0.05, 0.1, 0.2, 0.5, 1, 2, 5\}$ and $r \in \{0.25, 0.5, 0.75, 1, 1.25, 1.5, 2, 3\}$, 56 combinations in all, each run in both modes. The vehicle damping ratio is 5 % and the bridge damping ratio 0.3 %. The smooth road isolates the inertial interaction from roughness excitation, and the single-DOF vehicle makes r unambiguous. Fig. 13 maps four measures of the coupled-decoupled discrepancy over the (μ, r) grid.

At the lowest sampled frequency ratio, $r = 0.25$, increasing μ from 0.05 to 5 raises displacement NRMSE from 0.19 % to 3.30 %, bridge acceleration NRMSE from 1.14 % to 22.14 %, and body-acceleration NRMSE from 0.53 % to 18.96 %. This is a soft-suspension regime, not the rigid moving-mass limit. Near frequency tuning, dynamic errors can be large even for the lightest sampled vehicle. At $\mu = 0.05, r = 1$, the respective errors are 2.16 %, 17.20 %, and 76.75 %. Body-acceleration NRMSE reaches 660 % at $\mu = 5, r = 1$. The strong sensitivity of the dynamic outputs is consistent with the frequency-dependent interaction mechanisms discussed by Stoura and Dimitrakopoulos (2020a,b). Peak midspan displacement is less sensitive in this particular crossing: its absolute relative error is at most 3.45 % across the 56 cases. All cases converged without relaxation, with a maximum of 29 iterations at $\mu = 5, r = 3$. The coupled contact force remained compressive in all sampled cases (minimum total force/static weight = 0.842).

Response-specific screening. Table 9 gives explicit reporting targets and the sampled combinations satisfying them. The targets are chosen for comparing numerical responses; they are not design-code acceptance limits. Errors cover the common analysis window, including the 5 m approach, and use the coupled response as reference.

Contact-force accuracy must be checked separately from body acceleration. At $\mu = 0.05, r = 1$, the force RMS error divided by static weight is 1.50 %, and the peak-force error is 2.22 %, despite body-acceleration

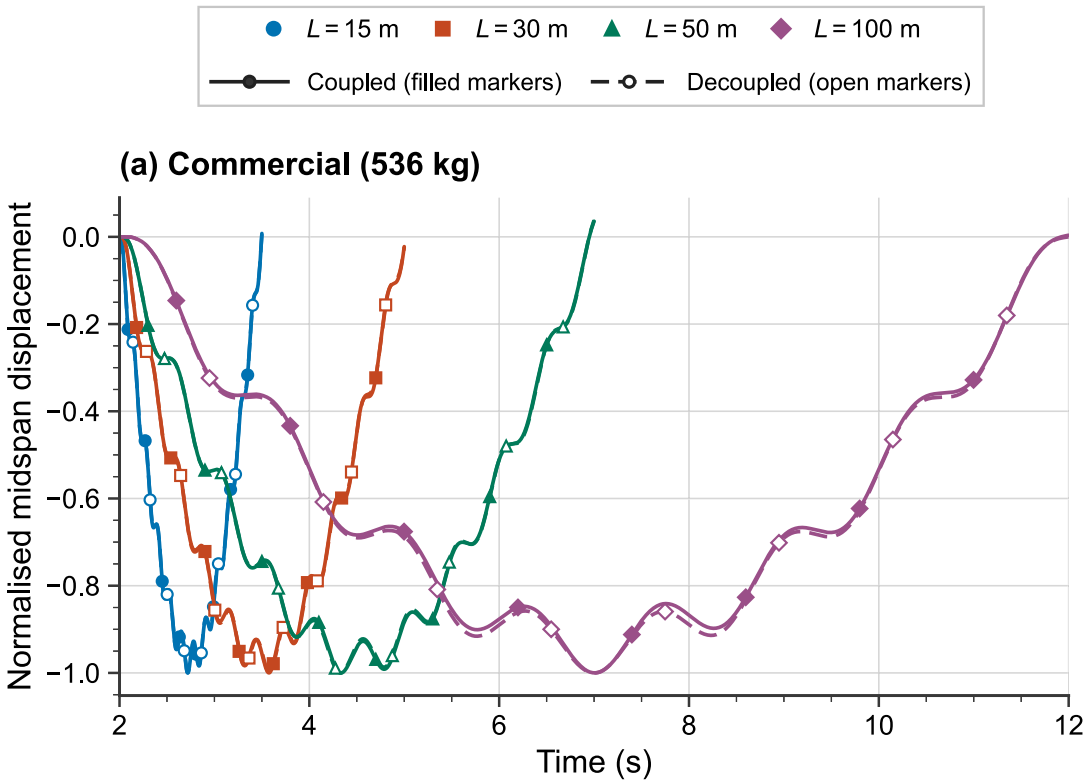

Fig. 9. Normalised bridge midspan displacement for the commercial vehicle across four spans (15 m, 30 m, 50 m, 100 m). Circle, square, triangle, and diamond markers identify the four spans, respectively. Solid lines with filled markers denote the coupled iterative analysis; dashed lines with open markers denote the decoupled (moving load) analysis. Markers indicate selected samples of the plotted histories.

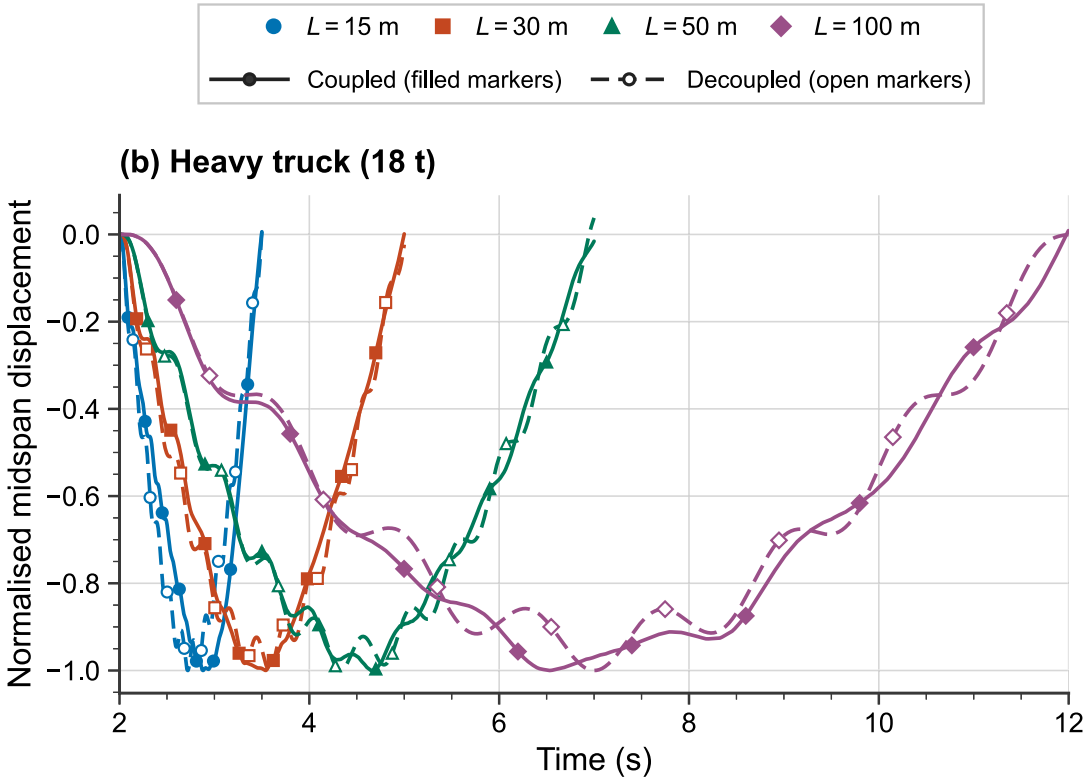

Fig. 10. Normalised bridge midspan displacement for the heavy truck across four spans. Span markers and line styles follow Fig. 9. Solid lines with filled markers denote the coupled iterative analysis; dashed lines with open markers denote the decoupled (moving load) analysis.

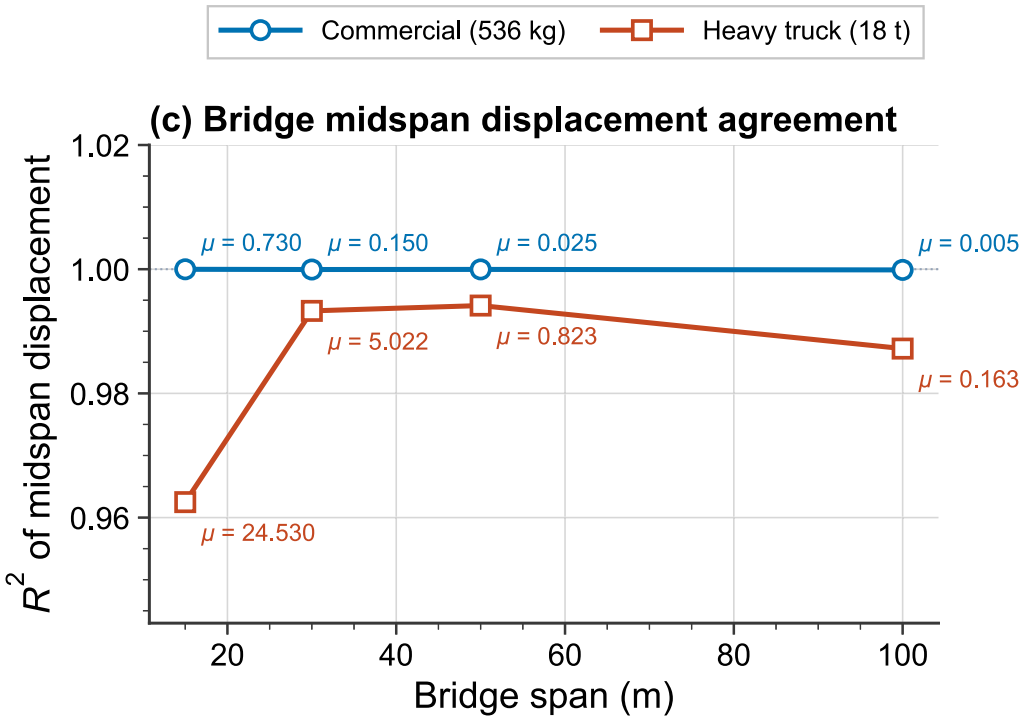

Fig. 11. Coefficient of determination R^2 for bridge midspan displacement between coupled and decoupled analyses as a function of span length, for the commercial vehicle (blue circles) and the heavy truck (red squares). Mass ratios μ are annotated next to each data point. Values close to 1 indicate close agreement.

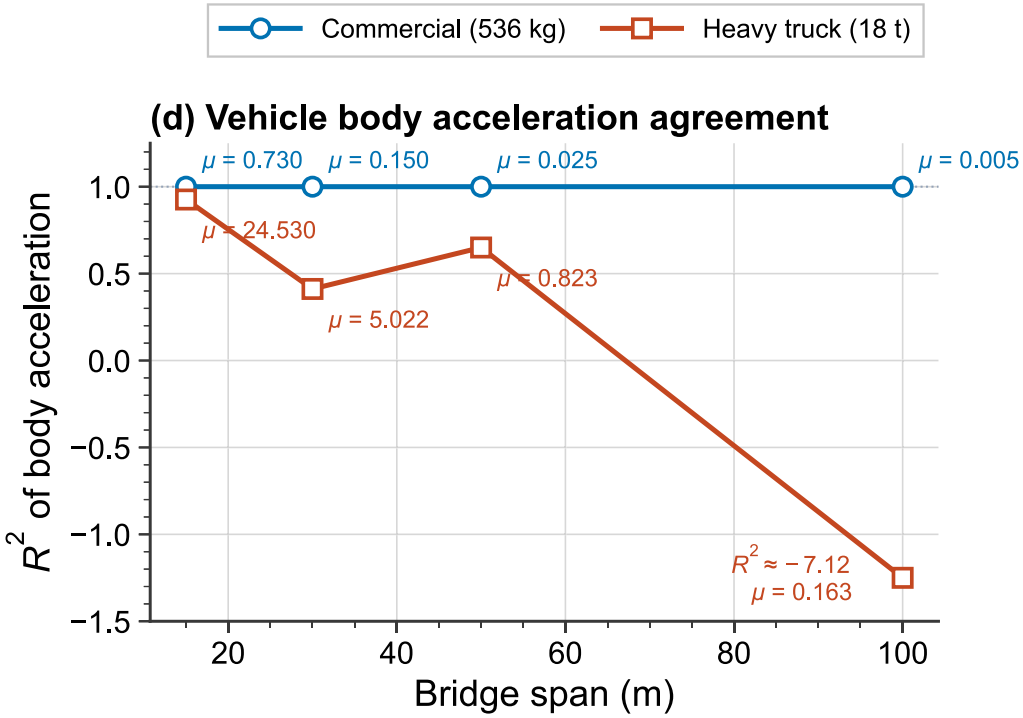

Fig. 12. Coefficient of determination R^2 for vehicle body acceleration between coupled and decoupled analyses as a function of span length, for the commercial vehicle and the heavy truck (both quarter-car composite models).

NRMSE of 76.75 %. At $\mu = 5, r = 1$, these force errors increase to 148 % and 294 %, respectively. Static-weight normalisation is useful for weighing applications because a range-normalised force error can be large even when the dynamic force range is small.

The table applies to this 30 m simply supported beam, 10 m/s crossing, smooth road, 0.3 % bridge damping, and 5 % single-DOF vehicle damping. It provides no tested bound below $\mu = 0.05$ or $r = 0.25$, between grid points, or for multi-DOF vehicles. Both quarter-car bounce ratios on this bridge (0.033 and 0.190) lie below the sampled grid and cannot be assigned a result by clamping them to its first column. Their bounce/hop frequencies, damping, and modal contributions require a separate assessment. The roughness and traffic Monte Carlo studies

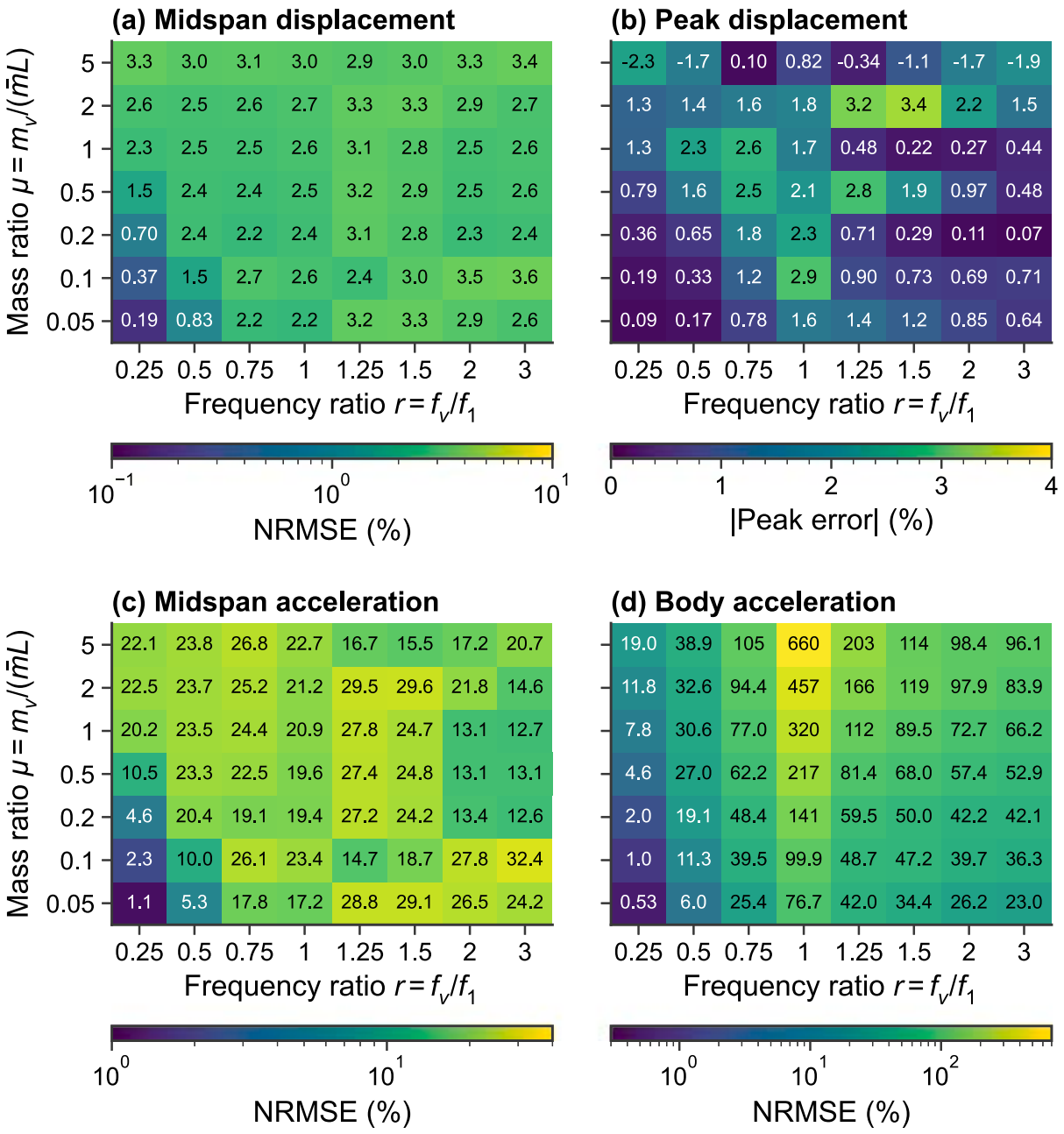

Fig. 13. Discrepancy between the decoupled (moving-load) and coupled analyses as a function of the mass ratio μ and the frequency ratio $r = f_v/f_1$ for a sprung-mass vehicle crossing the 30 m bridge at 10 m/s on a smooth road: (a) NRMSE of the bridge midspan displacement; (b) absolute error of the peak midspan displacement; (c) NRMSE of the bridge midspan acceleration; (d) NRMSE of the vehicle body acceleration. NRMSE is normalised by the range of the coupled response. Each cell is a sampled case; the colour map does not establish bounds between samples. In panel (b), colours show absolute error and cell labels retain the sign.

Table 9
Screening results on the sampled single-DOF grid. These are observations at the listed points, not continuous-domain guarantees.

Output	Reporting target	Sampled combinations meeting target
Peak bridge displacement	Absolute relative error below 3.5 %	All 56 sampled points
Bridge displacement history	NRMSE below 1 %; $R^2 > 0.998$	$r = 0.25$, $\mu \in \{0.05, 0.1, 0.2\}$; also $(\mu, r) = (0.05, 0.5)$
Bridge acceleration history	NRMSE below 5 %; $R^2 > 0.9$	$r = 0.25$, $\mu \in \{0.05, 0.1, 0.2\}$
Vehicle body acceleration	NRMSE below 5 %	$r = 0.25$, $\mu \in \{0.05, 0.1, 0.2, 0.5\}$
Contact-force history	RMS error divided by static weight below 1 %	20 of 56 points; the released records identify each point

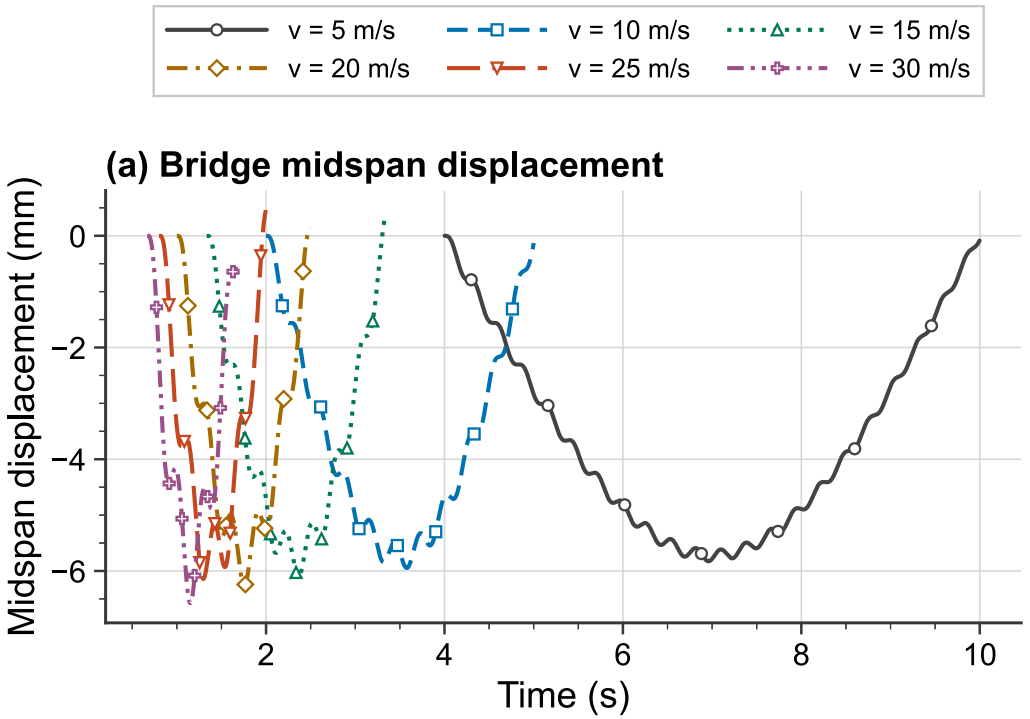

Fig. 14. Bridge midspan displacement for the 30 m bridge under the commercial quarter-car vehicle at six vehicle speeds (5, 10, 15, 20, 25, and 30 m/s), level R1 roughness. Line styles and marker shapes identify speed consistently in Figs. 14–17; markers are shown at selected samples for legibility.

below assess those two quarter-cars; they do not statistically validate every point or threshold in this map.

5.3. Effect of vehicle speed

The effect of vehicle speed on both bridge and vehicle responses is examined on the 30 m bridge with the commercial quarter-car vehicle under level R1 roughness. The vehicle speed is varied from 5 to 30 m/s (18 to 108 km/h), which covers the usual range of highway traffic. In dimensionless terms, the speed parameter $S = v/(2f_1L)$, which compares the loading frequency of the moving vehicle with the fundamental bridge frequency, ranges from 0.023 to 0.137 for this bridge ($f_1 = 3.63$ Hz). The study therefore covers the sub-resonant regime typical of highway traffic, far below the first critical speed $S = 1$, and the amplification observed below grows monotonically with S rather than peaking at a resonance condition.

Vehicle speed sets the loading frequency seen by the bridge: faster vehicles excite higher-frequency content and spend less time on the span. At low speeds (5–10 m/s) the bridge midspan displacement is close to the quasi-static deflection and the response is dominated by the first beam mode (Fig. 14). As speed increases, dynamic amplification appears: the peak midspan displacement and the free-vibration oscillations after the vehicle exits both grow with speed. The bridge midspan acceleration (Fig. 15) increases markedly with speed, because the moving load excites the bridge at higher frequencies. The vehicle body displacement (Fig. 16) shows the same trend: at higher speeds the vehicle traverses the bridge deflection profile faster, which produces larger oscillations. The vehicle body acceleration (Fig. 17) also grows with speed, driven by both the dynamic bridge response and the higher-frequency roughness excitation at elevated speeds.

5.4. Time-varying vehicle speed

The speed study above, like the rest of the parametric study, uses a constant speed, but the framework does not require one: the vehicle enters only through its axle position history $x_a(t)$ (Section 3.4), so acceleration and braking are prescribed by integrating a speed profile $v(t)$ into a position history and passing that array in place of $x_0 + vt$. Nothing else changes; in particular the roughness velocity input follows the instantaneous speed through $\dot{r} = v(t)\, r'(x_a)$. Fig. 18 demonstrates this with the heavy truck on the 30 m bridge under level R2 roughness for four crossings: constant 20 m/s, constant 10 m/s, braking from 20 to 10 m/s at -5 m/s^2 over exactly the span length, and accelerating from 10 to 20 m/s at $+5$ m/s^2. The same roughness realisation is used in all four cases.

The braking crossing produces the largest midspan displacement (221 mm, against 211 mm at constant 20 m/s and 210 mm at constant 10 m/s) and the largest midspan acceleration, because the truck enters at high speed, carrying the large dynamic contact force built up on the approach roughness at that speed, and then dwells longer over the middle of the span as it slows down. The accelerating crossing is intermediate (216 mm). The body acceleration reflects the roughness excitation at the instantaneous speed, decaying along the span in the braking case and growing in the accelerating case. The contact force on the bridge stays between 0.63 and 1.38 of the static axle load across the four cases, the lowest value occurring in the braking case shortly after entry. The crossing times were 1.5 s, 3.0 s, and 2.0 s for the constant 20 m/s, constant 10 m/s, and the two variable-speed cases, and the coupling iteration count was unaffected (at most 6 per step). The demonstration is kinematic: the longitudinal braking or traction force at the contact and the associated pitch moment, which enter the braking analyses of Law and Zhu (2005), are not transmitted to the deck by the vertical vehicle models used here, and the non-stationary random-vibration treatment of variable-speed crossings by Yin et al. (2010) would be the natural reference for a statistical study.

5.5. Road roughness effects

Road roughness has a strong effect on the dynamic component of both bridge and vehicle responses. Under level R1 roughness, the bridge and the vehicle body displacements stay close to the quasi-static deflection produced by the vehicle weight (Fig. 19b, c). Levels R2 and

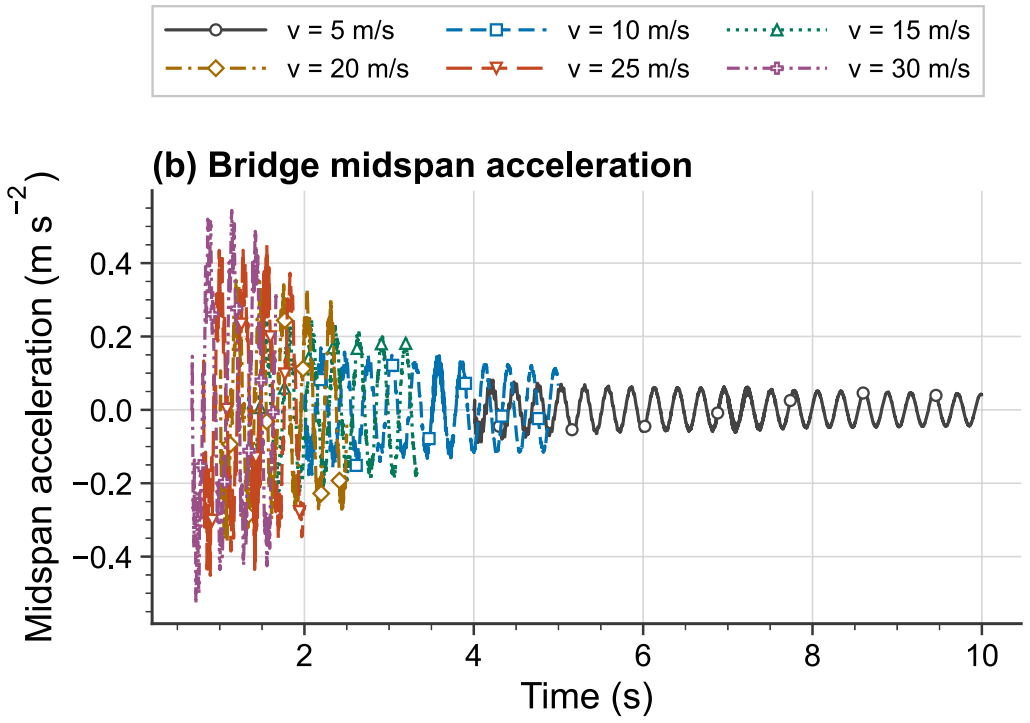

Fig. 15. Bridge midspan acceleration for the same six vehicle speeds.

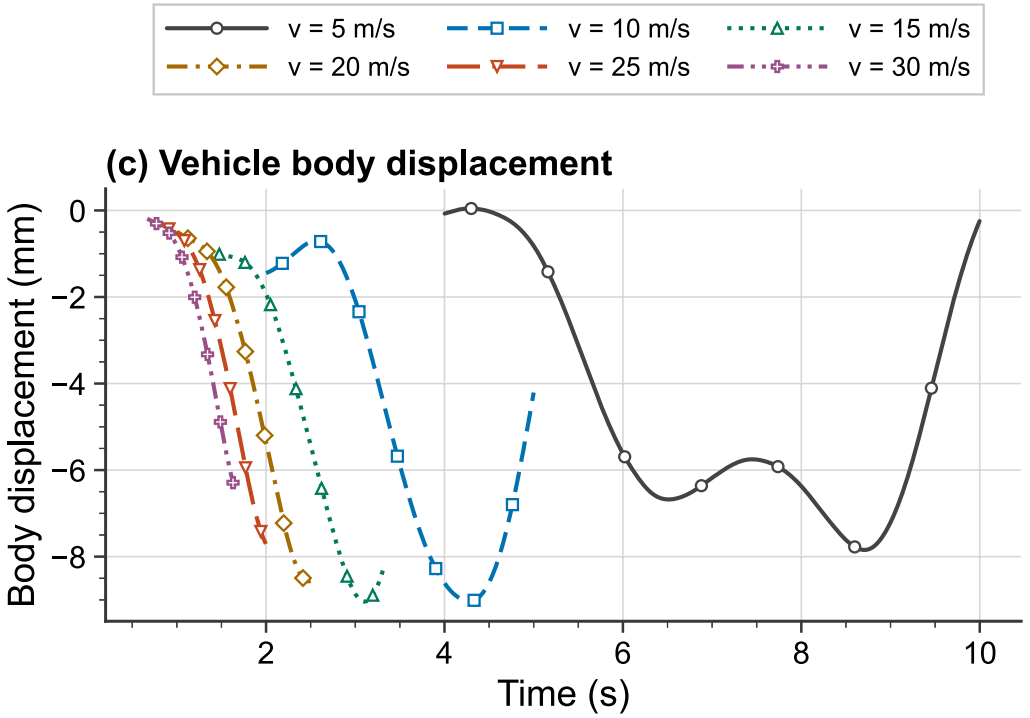

Fig. 16. Vehicle body vertical displacement for the same six vehicle speeds.

R3 introduce progressively larger dynamic oscillations, especially in the vehicle body, which is excited by the road profile through the suspension: the vehicle body acceleration amplitude under level R3 roughness is more than an order of magnitude larger than under level R1 (Fig. 19e). The bridge midspan acceleration (Fig. 19d) is much less sensitive to the roughness level for this lightweight vehicle, because the bridge response is dominated by its own modal content rather than by the roughness-induced contact forces. Heavier vehicles push more of that roughness signature into the bridge acceleration, which is the basis of using surface condition as an excitation source in indirect bridge monitoring (González et al., 2008; Yang et al., 2004a).

Repeating the roughness sweep with the heavy truck (18,000 kg, $\mu \approx 5$ on this bridge) confirms that the roughness level does not change the coupled-decoupled picture established by the mass ratio. For roughness levels R1, R2, and R3 the coupled and decoupled midspan displacements agree at $R^2 \approx 0.99$ (NRMSE about 3 % in all

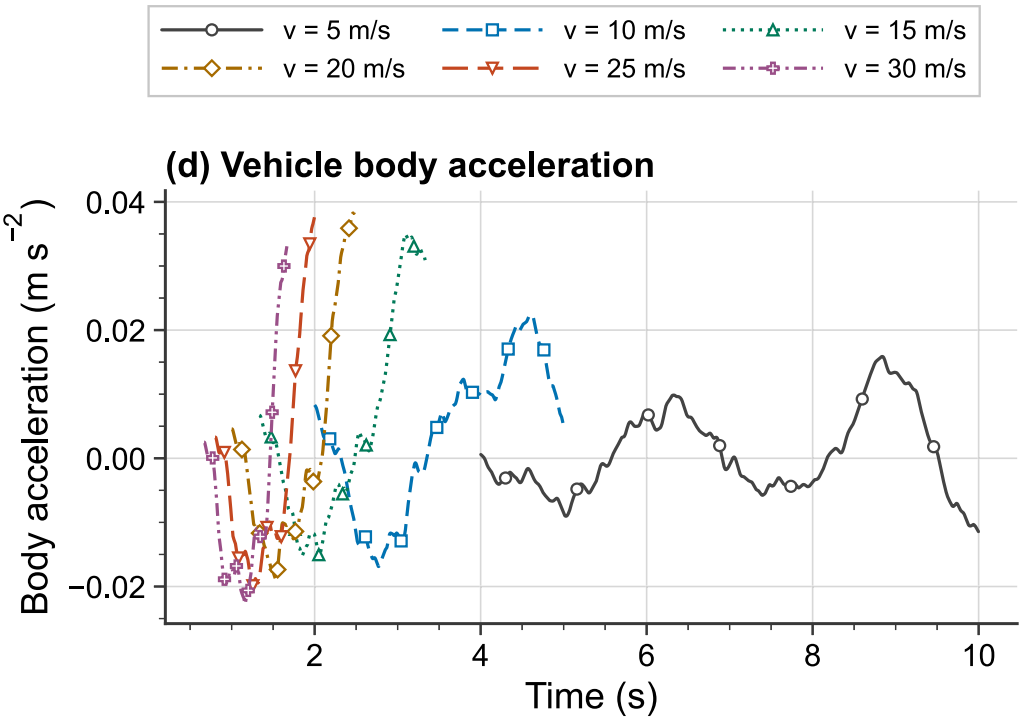

Fig. 17. Vehicle body vertical acceleration for the same six vehicle speeds.

three cases), while the midspan *acceleration* of the decoupled mode is essentially uncorrelated with the coupled solution at every class (R^2 near zero or negative). In other words, for a heavy vehicle the decoupled approximation fails on the dynamic (acceleration) content regardless of how smooth the surface is, because the missing inertial feedback, not the roughness excitation, is the dominant error source; smoothing the road does not rescue the approximation.

Statistical robustness. The roughness results above rest on one profile realisation per level. To test whether the conclusions depend on that draw, the roughness sweep was repeated for 20 independent realisations of each level (fixed seeds, released with the scripts), for both vehicles and both analysis modes, i.e., 240 additional crossings. Table 10 summarises the mean and standard deviation of the agreement metrics, and Fig. 20(a, b) shows the individual realisations. The spread is small compared with the separation between the two vehicles: for the commercial vehicle the displacement R^2 is 0.998 or higher in every realisation of every level, and for the heavy truck it lies between 0.981 and 0.996, with a displacement NRMSE of 2.9 %–3.3 % and a peak error of −5.4 to −6.5 % on average. The heavy truck's midspan-acceleration R^2 has a mean near zero, with individual values ranging from about −1.53 to 0.44 across the three levels, and its body-acceleration R^2 between 0.2 and 0.9. The realisation-to-realisation variability of the coupled response itself is modest for levels R1 and R2 (coefficient of variation below 2 % for the peak midspan displacement and below 3 % for the peak midspan acceleration) and grows to 4 % and 16 % for level R3. The minimum contact force over the full simulated crossing and approach/exit window stays above 0.90 of the static axle load for the heavy truck under levels R1 and R2 and above 0.65 under level R3, so no retained realisation reached zero contact force.

5.6. Effect of background traffic

The previous analyses considered a single vehicle in isolation. In practice bridges carry several vehicles at the same time, and the resulting background traffic changes the bridge response amplitude. This study checks whether background traffic also changes the relative accuracy of the decoupled mode. The 30 m bridge (Eshkevari configuration) is loaded with either the commercial vehicle or the heavy truck as the instrumented sensing vehicle. Background traffic is represented by the stochastic distributed-load surrogate of Sadeghi Eshkevari et al. (2020b), supplied through the external force channel $\mathbf{F}_{\text{ext}}$ of Algorithm 1: at every time step, non-negative random nodal forces are drawn independently from a uniform distribution at all bridge nodes and scaled so that their resultant equals the weight of n vehicles of 2000 kg each ($n = 0, 5, 10, 20$). The spatial distribution of the load therefore changes randomly from step to step while its resultant is constant. This surrogate reproduces the magnitude and broadband character of ambient traffic loading, but it does not travel across the bridge, has no axle structure or vehicle dynamics, and cannot interact with the bridge; it is a deliberate simplification that isolates the effect of additional loading amplitude on the coupled-decoupled agreement. Explicitly simulated multi-vehicle traffic is also supported by the framework (the fleet analysis of the next subsection uses it) at correspondingly higher computational cost, and micro-simulated traffic streams (Enright and O'Brien, 2013; O'Brien and Enright, 2011) can be converted into vehicle pools in the same way.

Background traffic increases both the bridge displacement and acceleration amplitudes substantially (Fig. 21a, b). The coefficient of determination R^2 between coupled and decoupled analyses (Fig. 21c) decreases with the number of background vehicles for both vehicle classes, with the largest drop between the isolated case ($n = 0$) and moderate traffic ($n = 5$). For the commercial vehicle, R^2 stays close to unity at every traffic level. For the heavy truck, R^2 keeps decreasing as traffic grows, so the agreement becomes progressively worse. The deterioration is driven by the heavier total loading, which produces larger bridge deflections and therefore larger dynamic contact forces that the decoupled mode ignores. The ordering between the two vehicle classes is preserved at every traffic level: the heavy truck always gives a lower R^2 than the commercial vehicle, but their differing suspension and axle-hop properties prevent attributing that separation to mass ratio alone.

Statistical robustness. Because the surrogate is random, the study was repeated for 20 independent traffic realisations at each level $n = 5, 10, 20$ with the roughness profile held fixed, for both vehicles and

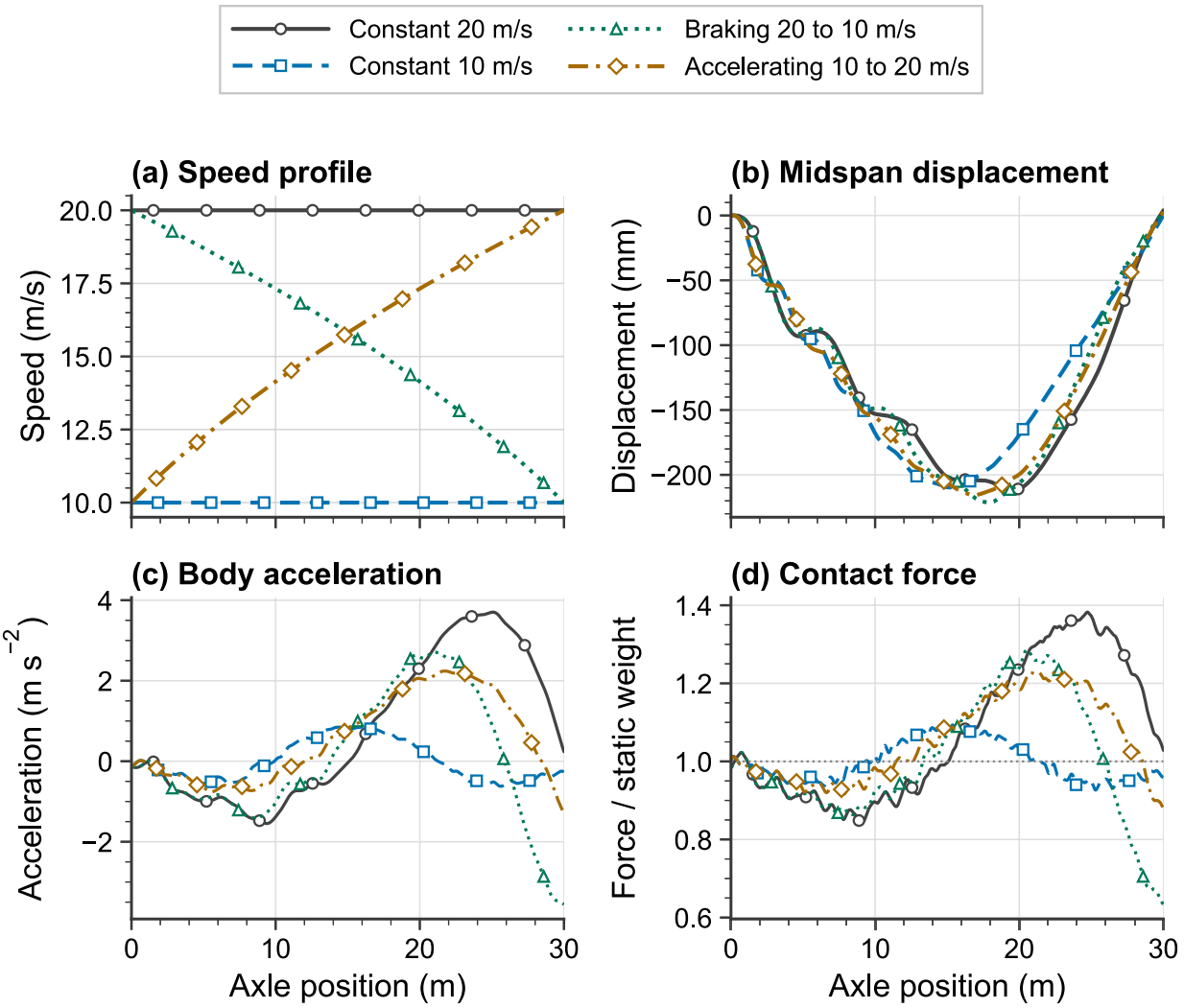

Fig. 18. Crossings of the 30 m bridge by the heavy truck under level R2 roughness with constant and time-varying speed, plotted against the axle position: (a) speed profile; (b) bridge midspan displacement; (c) vehicle body acceleration; (d) contact force normalised by the static axle load.

Table 10
Monte Carlo statistics (mean ± standard deviation over 20 roughness realisations) of the agreement between the coupled and decoupled analyses on the 30 m bridge at 10 m/s. NRMSE is normalised by the range of the coupled response; the peak error refers to the midspan displacement; $F_{\min}/W$ is the minimum contact force over the full simulation window divided by the static axle load in the coupled analysis.

Vehicle	Level	R^2 disp.	NRMSE disp. (%)	Peak error (%)	R^2 acc.	$F_{\min}/W$
Commercial	R1	1.0000 ± 0.0000	0.11 ± 0.03	−0.09 ± 0.07	0.999 ± 0.001	0.997 ± 0.001
Commercial	R2	1.0000 ± 0.0000	0.22 ± 0.07	−0.08 ± 0.29	0.996 ± 0.003	0.994 ± 0.001
Commercial	R3	0.9994 ± 0.0004	0.75 ± 0.27	−0.11 ± 1.20	0.947 ± 0.051	0.978 ± 0.004
Heavy truck	R1	0.9926 ± 0.0003	2.91 ± 0.05	−5.40 ± 0.25	0.04 ± 0.04	0.935 ± 0.003
Heavy truck	R2	0.9924 ± 0.0011	2.94 ± 0.18	−5.54 ± 1.00	0.01 ± 0.16	0.924 ± 0.009
Heavy truck	R3	0.9895 ± 0.0044	3.34 ± 0.62	−6.52 ± 3.80	−0.07 ± 0.40	0.800 ± 0.063

both modes (240 additional crossings; Fig. 20(c, d)). For the commercial vehicle the displacement R^2 is 0.9989 ± 0.0000 at every traffic level and the two modes give the same peak displacement to within 10^{-9}, because the traffic load, which dominates the response, is identical in the two modes. These are full-history peaks, which can be governed by traffic before the vehicle arrives; their equality is not a bound on the error during the crossing. For the heavy truck the displacement R^2 falls from 0.926 ± 0.005 (n = 5) to 0.758 ± 0.016 (n = 10) and 0.493 ± 0.030 (n = 20), the displacement NRMSE grows from 7.5 ± 0.3 % to 17.1 ± 0.5 %, and the decoupled peak displacement exceeds the coupled one by 5.4 ± 0.5 %, 14.8 ± 0.7 %, and 21.4 ± 0.8 %. The standard deviations are an order of magnitude smaller than the changes with n, so the trend of Fig. 21(c) is not an artefact of one realisation. The sign of the peak error is also informative: under broadband traffic excitation the coupled heavy truck reduces the bridge response, acting as the additional damping described in Section 2.3, whereas the decoupled mode cannot represent this effect and overpredicts the response.

5.7. Multi-span bridge configuration

The framework supports multi-span continuous bridges through user-defined intermediate supports. The capability is demonstrated on a two-span bridge crossed by a fleet of ten vehicles. The fleet is built

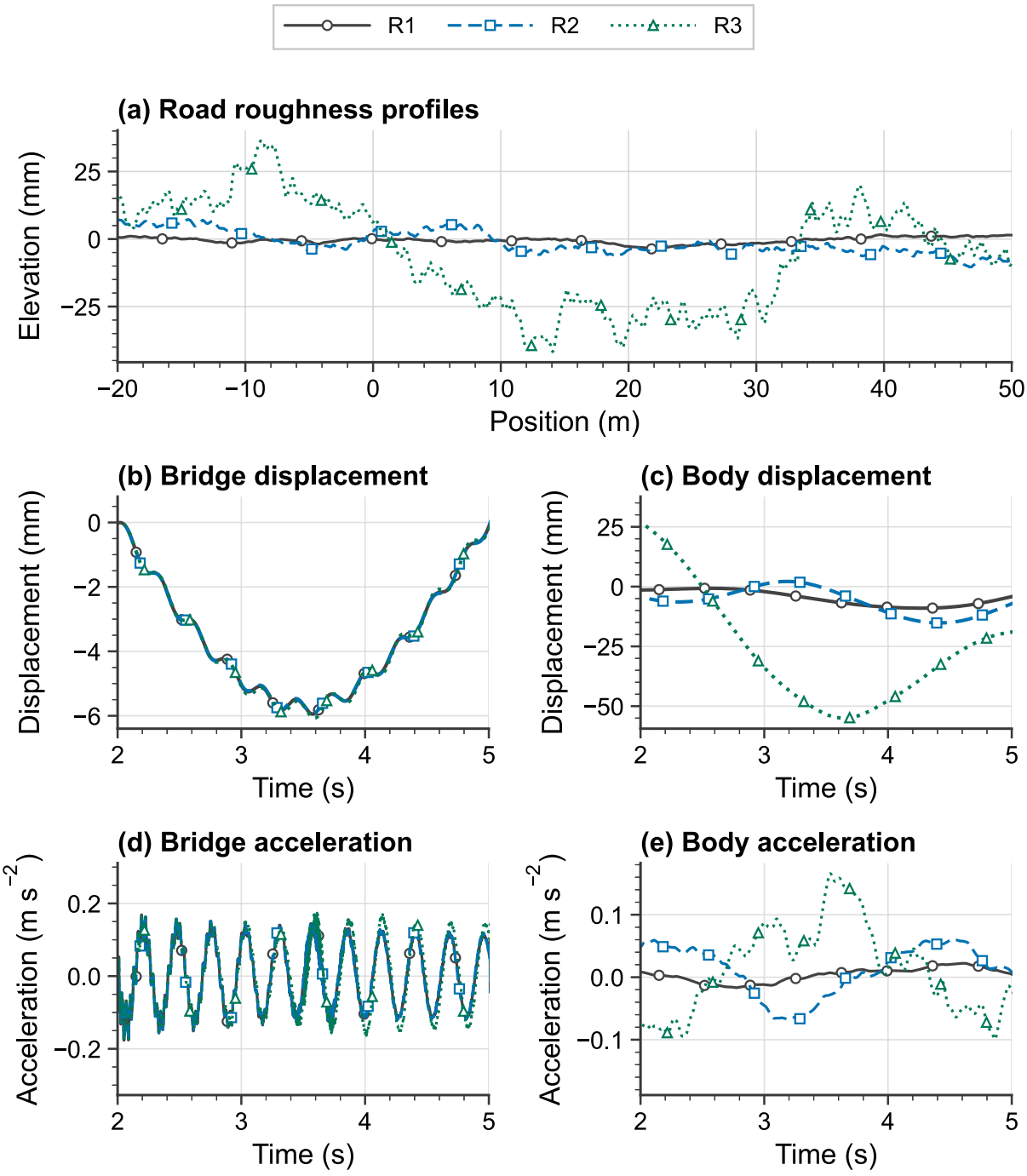

Fig. 19. Effect of road roughness on bridge and vehicle response (30 m bridge, commercial quarter-car vehicle). (a) ISO 8608 roughness profiles for roughness levels R1, R2, and R3. (b) Bridge midspan displacement. (c) Vehicle body vertical displacement. (d) Bridge midspan acceleration. (e) Vehicle body vertical acceleration. Line styles and marker shapes identify roughness levels consistently across all panels.

by perturbing a base two-axle half-car with pitch (comp2). Truncated normal factors in $[0.7, 1.3]$ scale its mass properties and, with a separate common factor, its suspension stiffness and damping. The suspension properties therefore vary together rather than independently. Initial positions are distributed along the approach. Each vehicle has a constant speed drawn within 14–26 m/s around a 20 m/s nominal value; the ten speeds are not identical.

The two-span case (Fig. 22) shows that the framework handles continuous bridges with multiple vehicles. The displacement snapshots have the characteristic shape of a continuous beam under moving loads, with the inflection point at the intermediate support and alternating deflections in the two spans as the vehicles cross them. This case is a capability demonstration rather than a validation: no independent reference is available for this configuration, and quantitative validation of the multi-span and multi-vehicle features against published or experimental data is identified as future work.

6. Discussion

The validation cases and the parametric studies above support a few observations about the framework and about the VBI problem itself.

Using OpenSees for both subsystems makes the models inspectable and allows existing linear bridge-modelling components to be reused. Model construction, interface-node selection, and storage of all active

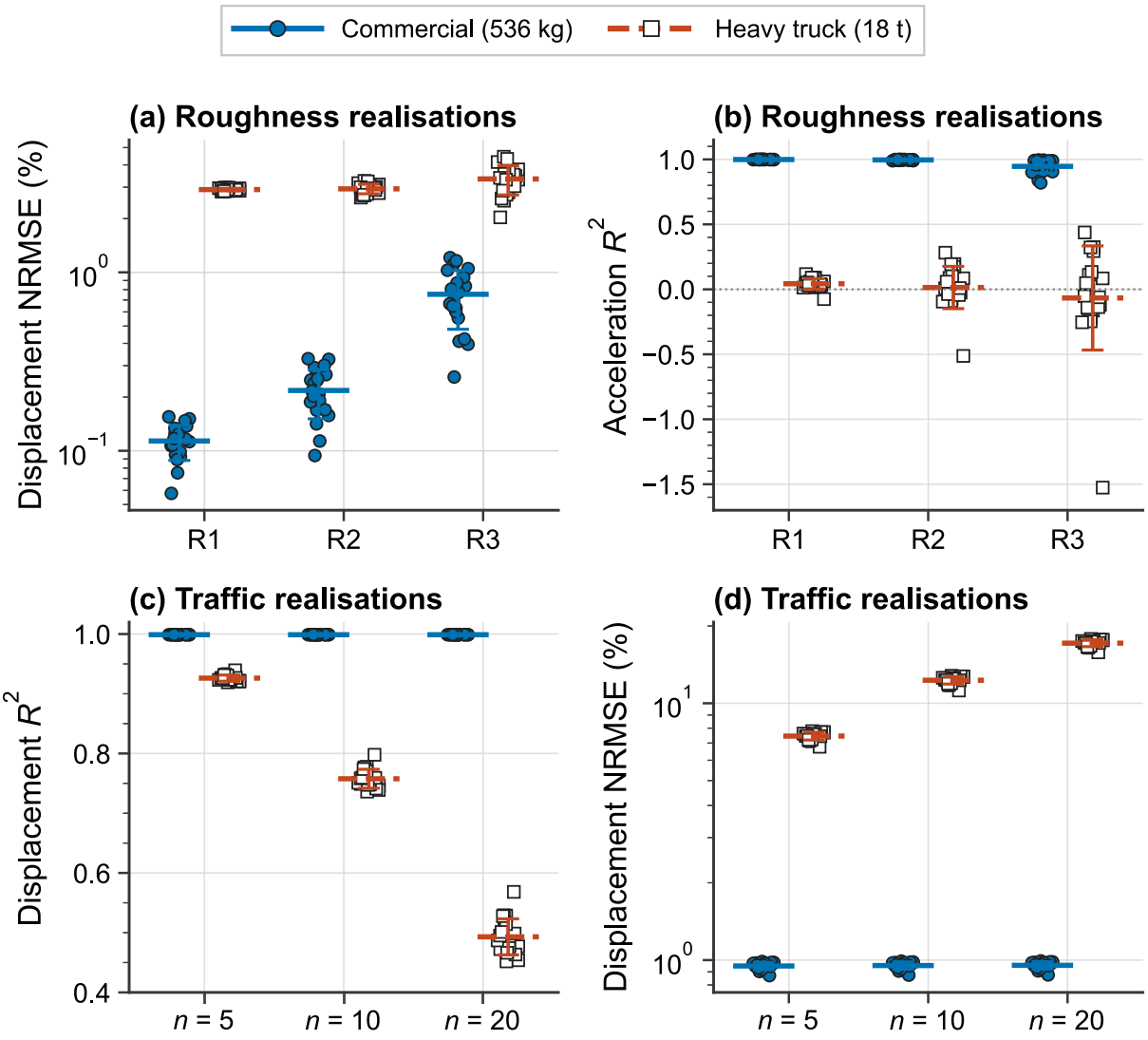

Fig. 20. Monte Carlo spread of the coupled-decoupled agreement on the 30 m bridge (20 realisations per case; filled circles and open squares are individual realisations for the commercial vehicle and heavy truck, respectively; horizontal bars show means and error bars show ± one standard deviation): (a) NRMSE of the midspan displacement and (b) R^2 of the midspan acceleration over roughness realisations of roughness levels R1, R2, and R3; (c) R^2 and (d) NRMSE of the midspan displacement over background-traffic realisations with $n = 5$, 10, and 20 vehicles (Section 5.6).

nodal states must be extended together when a pier, track, or foundation adds degrees of freedom. The coupling pattern can remain the same, but the current deck-only state arrays are not a general substructure interface. Rebuilding separates bridge and vehicle domains and simplifies the implementation; it neither removes time-integration error nor preserves nonlinear material history. Persistent domains with reliable rollback to the last converged state are needed for path-dependent extensions.

The decoupled-mode studies show why mass ratio alone is insufficient. The span sweep changes bridge frequency, mass ratio, and traversal time together, and the two quarter-cars also differ in suspension damping and axle-hop frequency. It cannot isolate a single cause of vehicle-class dependence. The controlled single-DOF map in Section 5.2 isolates mass and frequency ratios at fixed speed and damping and demonstrates the sensitivity of dynamic outputs near frequency tuning. The Monte Carlo checks independently describe variability for the two quarter-cars on the 30 m bridge; they do not statistically validate every point of the frequency-ratio map or its extension to other vehicle models.

The speed study shows that higher vehicle speeds produce larger dynamic amplification in both bridge and vehicle responses, in line with the well-known speed parameter effect for moving-load problems. The roughness study shows that the surface condition has a strong effect on the vehicle body (level R3 acceleration is more than an order of magnitude larger than level R1), while the bridge midspan response is much less sensitive to roughness for this lightweight vehicle. The traffic study shows that background traffic weakens the coupled-decoupled agreement: the heavy-truck R^2 decreases visibly as the number of background vehicles grows from 0 to 20, while the commercial-vehicle R^2 stays close to one. The decrease is caused by the additional loading, which amplifies bridge deflections and the associated dynamic contact forces that the decoupled mode ignores (González et al., 2008; O'Brien and Keenahan, 2015).

Releasing the framework as open source also addresses a long-standing gap in the VBI literature. The theory is mature, but the lack of shared, validated, and documented implementations has led to repeated re-implementation and made it hard to reproduce published results. Building on a widely used platform and shipping a complete Python implementation together with the benchmark configurations lowers the

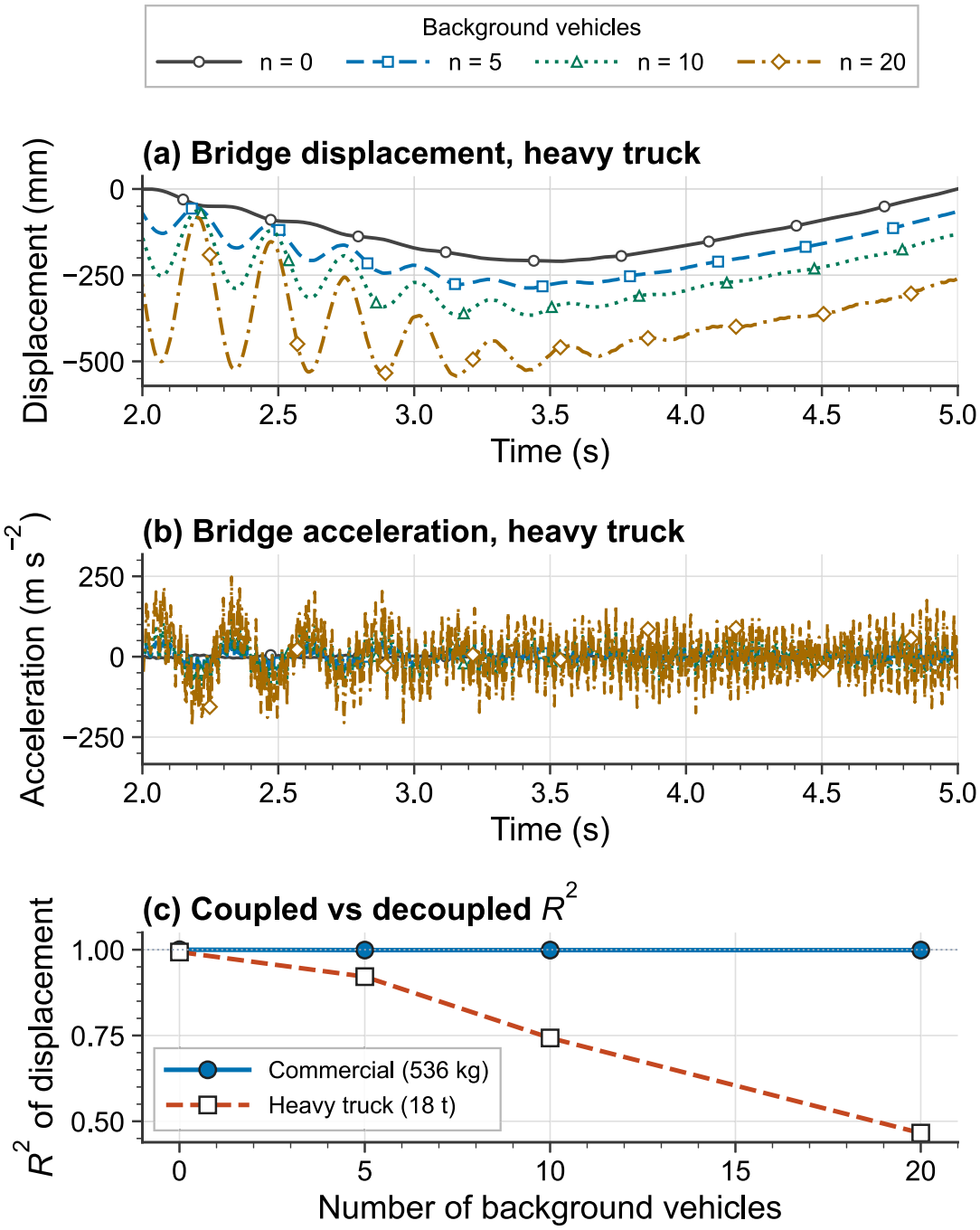

Fig. 21. Effect of background traffic on bridge response (30 m bridge, heavy truck, coupled analysis). (a) Bridge midspan displacement with increasing traffic levels. (b) Bridge midspan acceleration with increasing traffic levels. (c) Coefficient of determination R^2 between coupled and decoupled analyses as a function of the number of background vehicles, for both vehicle types. Panels (a) and (b) share the same line styles and marker shapes for each traffic level.

barrier of entry for researchers and engineers working on VBI analysis and drive-by bridge monitoring.

6.1. Computational performance

All timings below were measured on a standard laptop (single core, Python 3.8, OpenSeesPy 3.3.0.1.1). These are recorded single-run timings; the three sizes are different model cases and no timing uncertainty or end-to-end persistent coupled solver is claimed. For the Benchmark 1 configuration with 250 beam elements and a single quarter-car at 500 Hz, the coupled mode costs 9.5 ms per time step and the decoupled mode 2.5 ms per step, a factor of about four: the decoupled mode solves the bridge once and the vehicle once, whereas the coupled mode rebuilds and re-solves both subsystems at every iteration (two to five iterations per step at $\epsilon_{\text{tol}} = 10^{-12}$, fewer at engineering tolerances). The cost grows nearly linearly with the number of bridge elements, from

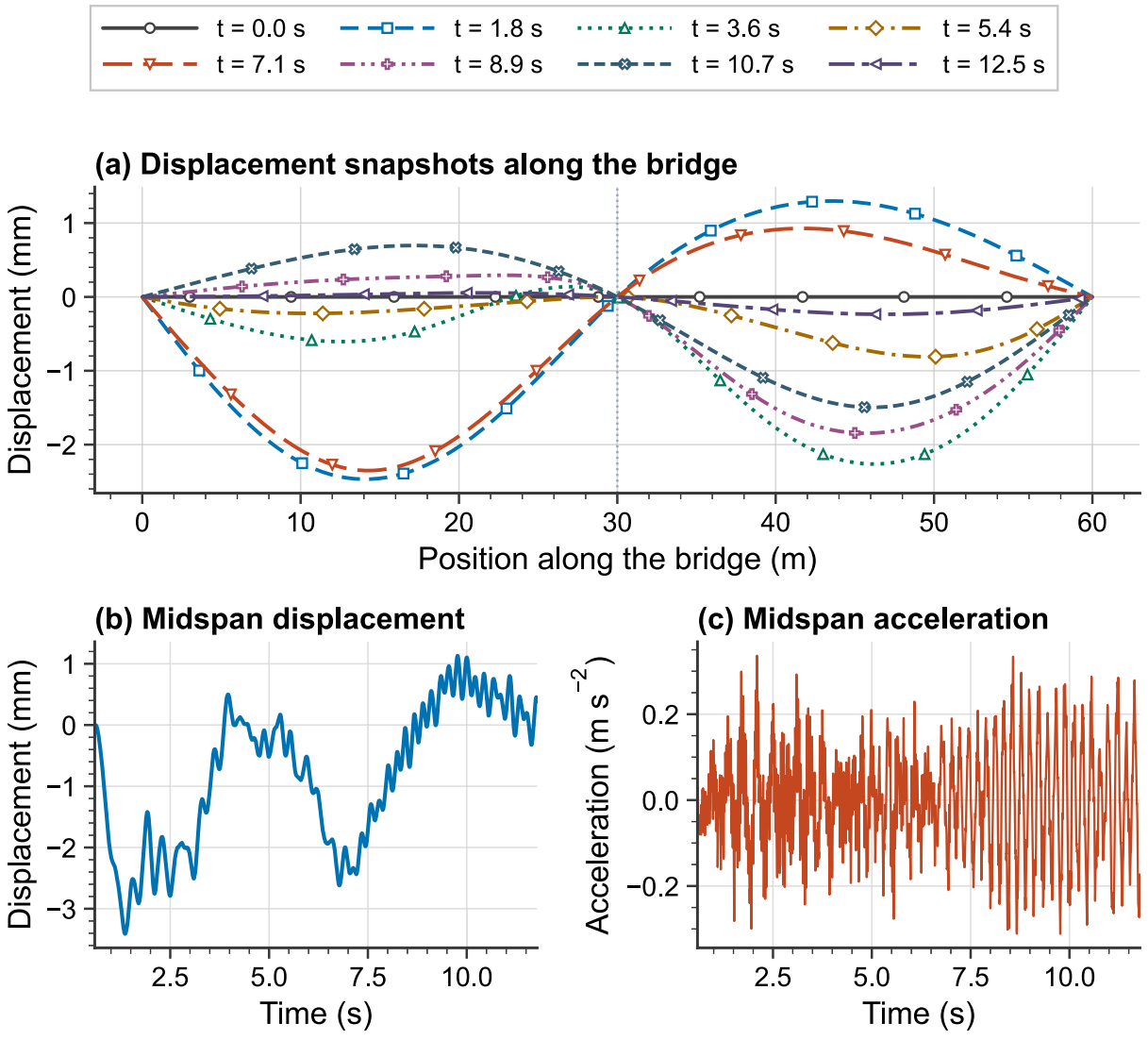

Fig. 22. Two-span continuous bridge (2 × 30 m) under a fleet of 10 randomly generated vehicles: (a) bridge displacement profiles over the full span at eight time instants, identified by line styles and marker shapes; (b) midspan displacement time history of the first span; (c) midspan acceleration time history of the first span.

4 ms per step at 100 elements to 36 ms per step at 1000 elements. In absolute terms, every benchmark runs in roughly 8–90 s in the test environment. These single-run timings depend on hardware and concurrent system load; they are not portable performance guarantees.

Where the time goes. Profiling the coupled Benchmark 1 run (1252 steps, 4976 bridge solves) with `cProfile` attributes 42 % of the profiled runtime to OpenSees model construction calls (node, element, mass, load pattern, time series, and state-restoration commands issued at every rebuild), 20 % to the transient solves themselves, 5 % to response extraction, 1 % to the vehicle eigenvalue analysis, and the remaining 32 % to Python bookkeeping in the coupling layer (force mapping, interpolation, list conversions, and history storage). The rebuild-per-step strategy is therefore the largest single cost but not the whole overhead: removing this measured fraction would imply an idealised speedup of about 1.7 if all other costs remained unchanged; this is not a measured end-to-end persistent-solver speedup.

Comparison with a persistent bridge domain. To quantify the achievable saving, a persistent variant of the bridge step was implemented in which the OpenSees bridge domain (nodes, elements, mass, damping, and analysis objects) is created once and, at every call, only the load pattern is replaced and the committed nodal state is reset. The tests use the Benchmark 1 moving static load on the 25 m bridge at 250 and 1000 elements, and on the 30 m parametric bridge at 300 elements. On this bridge subsystem alone, the persistent variant reproduces the rebuild variant to a relative difference below 10^{-9} and costs 1.18 ms per bridge step against 2.01 ms at 250 elements, 1.33 ms against 2.43 ms at 300 elements, and 4.74 ms against 8.24 ms at 1000 elements, speedups of 1.71, 1.83, and 1.74, respectively; a one-shot solve of the whole prescribed load history in a single model (a separate bridge-only baseline) costs 0.35, 0.44, and 1.59 ms per step respectively and provides an additional comparison, not a proven lower bound. The persistent variant is not adopted in the released framework for a structural reason: OpenSeesPy exposes a single domain, and the vehicle solver wipes and rebuilds that domain at every call, which would destroy a persistent bridge. Making the whole framework persistent therefore requires either both subsystems to live in one domain, with the two solves advanced alternately by resetting committed states, or the vehicle to be integrated outside OpenSees. Both are feasible, a

nonlinear implementation additionally needs material-state rollback between trial iterations; nodal resets alone are insufficient for path-dependent models (Section 6.4), and the persistent bridge step is released with the code as a prototype. The framework is comfortably fast for research and design studies, though not for hard real-time use. Each simulation is single-threaded and self-contained, so parameter sweeps and Monte Carlo studies can run in parallel with one analysis per core and no shared state. The 112 analyses of the frequency-ratio map and the 480 Monte Carlo crossings were run as independent processes.

6.2. Practical guidance for users

The validation and parametric results translate into concrete guidance for applying the framework.

Choosing between coupled and decoupled modes. Use the output-specific targets and sampled results in Table 9 as initial screening evidence. For a new case, evaluate the vehicle-to-bridge mass ratio and relevant bounce, pitch, and hop frequency ratios together with modal damping, road input, speed, and traffic loading. Compare both solution modes for the actual output and time window needed. A small peak-deflection error does not establish accurate acceleration or axle force, and the single-DOF table does not define a universal vehicle-class threshold. The heavy quarter-car studies illustrate the need for coupled analysis of its dynamic outputs. When the decoupled approximation meets the chosen target, it requires one bridge and one vehicle step at each time increment without coupling iteration (Section 6.1).

Choosing a vehicle model. The single-axle models suffice for bridge-side quantities under light vehicles. The quarter-car composite model is the standard choice for drive-by monitoring studies because it separates body bounce from axle hop. The two-axle models with pitch are needed when the axle spacing is not small relative to the span, when pitch couples into the measured body response, or when individual axle forces matter. Table 11 gives the complete OpenSees topology of each type.

Numerical settings. A convergence tolerance of 10^{-6} on the displacement residual reproduces the 10^{-12} reference solutions to within a relative deviation of 10^{-9} while saving a third of the iterations (Section 4.5); 10^{-12} is used in this paper only to make the benchmark comparisons independent of the iteration error. Element sizes of $L/250$ or finer and sampling rates of 500 Hz or higher reproduced the reference responses to graphical accuracy in the convergence studies; both should be confirmed per problem by one refinement step.

Interpreting warnings. A wheel-uplift warning means the total contact force at an axle reached zero; results beyond that instant do not resolve physical separation and impact, and the case should be re-examined (lower speed, smoother profile, or a dedicated contact model). Iteration counts are returned per time step; sustained growth of the count signals that the mass ratio or the loading is pushing the fixed-point iteration towards its limits.

Extending the framework. The coupling layer only exchanges nodal displacements, velocities, and forces, so bridge models may use compatible linear OpenSees elements. Extra subsystem DOFs require additional state storage; path-dependent elements require a persistent domain with committed-state rollback. New vehicle topologies are added by defining the node-element layout and the imposed-motion pattern, mirroring the templates in the Appendix.

6.3. Extensibility: Substructures, railway systems, and external excitation

Three questions arise naturally for a framework that presents itself as general: can the bridge model include piers, bearings, and foundation flexibility; can the same scheme handle railway bridges with a track layer and multi-body trains; and can environmental excitation such as earthquakes or wind be applied. The answer follows from the interface described in Section 3.1: the coupling reads deck-node displacements and velocities and applies deck-node forces, and everything else lives inside the bridge and vehicle construction routines.

Substructures and foundations. Fig. 23 demonstrates the first point with the Benchmark 1 configuration in which the two rigid supports are replaced by vertical springs to ground of stiffness k_{sup}, representing bearing, pier, or foundation flexibility, with no change to the coupling layer or to the vehicle. A stiffness of 10^9 N/m (of the order of elastomeric bearings on stiff piers) lowers the first frequency from 2.084 to 2.075 Hz and raises the peak midspan displacement by 0.8 %; 10^8 N/m lowers it to 2.00 Hz and raises the peak by 8%; and 2×10^7 N/m, a soft foundation, lowers it to 1.73 Hz and raises the peak by 46 %, with 1.0 mm of support settlement under the 1.2 t vehicle. The coupling iteration count was unchanged (at most 4 per step). Piers modelled as beam–columns, pile groups as lumped-parameter soil models (Bucinskas and Andersen, 2020), and displacement-dependent bearings are added in the same place, the bridge construction routine, and the interface nodes must remain identifiable and all added active DOFs must be included in the state restored between solves. Nonlinear substructure elements are subject to the caveat on path-dependent state discussed in Section 6.4.

Railway bridges and trains. A track layer (rails on discrete pads, sleepers, and ballast) is a second beam or a set of springs above the deck and belongs to the bridge construction routine; the rail nodes then become the nodes seen by the coupling, and the deck, piers, and foundations sit below them. A multi-body train (car body, bogies, wheelsets) is a vehicle topology with more nodes and elements above the contact nodes and more contact nodes per vehicle, and several vehicles in sequence are already supported by the vehicle pool. The coupling pattern can therefore be extended to the vertical train-track-bridge problem in the planar sense of Cheng et al. (2001) and Xia and Zhang (2005); what it does not offer is the three-dimensional lateral wheel-rail contact and the nonlinear Hertzian normal contact of Antolín et al. (2013) and Montenegro et al. (2015), which require additional contact kinematics, unilateral contact and re-contact handling, and a compatible nonlinear solution strategy. No railway case has been validated here; the statements above concern the architecture, not demonstrated accuracy.

External excitation. Prescribed vertical nodal-force histories can use the existing additive force channel. Uniform vertical seismic excitation requires a consistent reference frame. With bridge coordinates relative to the ground, the bridge receives $-\mathbf{M}_b \boldsymbol{\iota}_b \ddot{u}_g$. Either the vehicle is also solved in relative coordinates with $-\mathbf{M}_v \boldsymbol{\iota}_v \ddot{u}_g$, or its absolute contact displacement and velocity include both u_g and $\dot{u}_g$. Horizontal or spatially varying support motions require corresponding bridge and vehicle DOFs, a suitable excitation pattern, and retention of the complete subsystem state. Prescribed wind buffeting can be supplied as external nodal forces; motion-dependent aerodynamic forces require an additional force-evaluation callback and convergence checks within the iteration (Cai and Chen, 2004; Kim et al., 2011; Xu and Guo, 2003; Zeng and Dimitrakopoulos, 2016). These are proposed extensions; no seismic, wind, or railway validation is claimed here.

6.4. Limitations

The present implementation has the following limitations.

Planar analysis and single-track profile. The framework is restricted to two-dimensional (in-plane) analysis and ignores lateral and torsional dynamics of both the bridge and the vehicle. The box cross-sections used in the parametric study (Table 7) therefore enter the model only through their flexural rigidity EI and distributed mass: cross-sectional distortion, warping, and torsion of the box girder are not represented. The same restriction applies to the vehicles: left and right

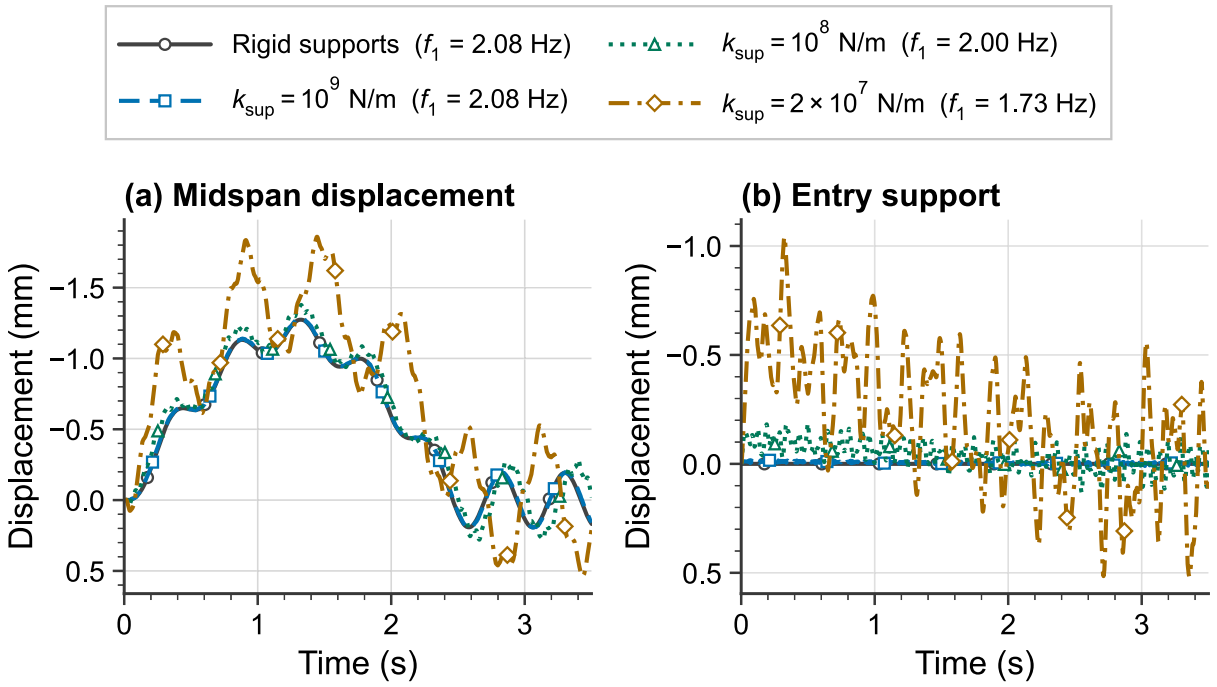

Fig. 23. Benchmark 1 configuration (25 m beam, 1.2 t sprung mass at 10 m/s) with the rigid supports replaced by vertical springs of stiffness k_{sup} to ground: (a) midspan displacement; (b) vertical displacement of the entry support. The coupling layer and the vehicle are unchanged.

wheels are not distinguished, a single-track roughness profile excites both sides identically, and roll dynamics cannot develop. The practical consequences are that (i) the transverse position of the vehicle in the carriageway, which governs the share of the load carried by each girder and the torsional response of a real deck (Huang et al., 1992; Kim et al., 2005), is not a parameter of the model, so the planar results correspond to a load applied at the shear centre of an equivalent beam; (ii) the roll excitation produced by different left and right wheel paths, which contributes to the body acceleration measured in drive-by studies and to the wheel-load redistribution exploited in B-WIM (Zhao et al., 2014), is absent; and (iii) eccentric loading, curved bridges, and multi-lane traffic require a three-dimensional extension in which the deck is a grillage or shell model, the vehicle has roll and independent wheel paths, and two roughness profiles are generated with the appropriate cross-correlation. The interface of Section 3.1 does not change in such an extension, but the mapping of contact forces to deck nodes and the interpolation of deck motion become two-dimensional.

Euler–Bernoulli beam theory. Shear deformation is neglected. For deep sections or span-to-depth ratios below about 10, Timoshenko beam elements would be more appropriate; they can be substituted directly because the coupling layer only reads nodal displacements and applies nodal forces.

Linear subsystems and the rebuild-per-step strategy. All analyses here use linear bridge and vehicle models, and this is a material limitation rather than a matter of configuration. OpenSees is attractive precisely for nonlinear structural analysis, but the rebuild-per-step strategy restores the committed state through nodal displacements, velocities, and accelerations only. This is a complete description of the state for elastic elements, and it is what makes the stateless exchange of Section 3 possible, but it does not carry path-dependent material state (plastic strains, damage variables, hysteretic bearing states, gap or friction states) from one step to the next. A nonlinear bridge or substructure would therefore be re-initialised on its elastic branch at every step and would give wrong results. Supporting nonlinear subsystems requires a persistent OpenSees domain (Section 6.1) or explicit bookkeeping of the committed material state, and, on the algorithmic side, safeguards for the fixed-point iteration, which currently has an iteration cap of 100 but no relaxation; for softening systems the iteration count can grow or the iteration can fail to converge, and under-relaxation (for example, Aitken acceleration) is the natural remedy (Stoura et al., 2021). The framework in its released form should be regarded as linear-elastic on both sides of the interface. **Point contact, hard cut-off, and re-contact.** The tyre-road interface is a point contact with a linear spring-dashpot. At every coupling iteration the total contact force (static axle load plus dynamic component) is checked: if it becomes tensile, it is set to zero for that time step, so the bridge is never pulled upward, while the vehicle continues to receive the bridge-surface motion as base excitation. This treatment removes the tensile-force artefact but is not a contact model, and three consequences follow. First, the transition is a hard cut-off, so the contact force history has a slope discontinuity at separation that can excite the tyre-hop mode spuriously. Second, during a separation the vehicle should physically be in free flight, whereas the model keeps its contact node attached to the surface, so the computed response during and after separation cannot be interpreted as a physical free-flight solution. Third, re-contact impact, which can produce large dynamic wheel loads, is not modelled, because the contact stiffness is linear and there is no penetration or restitution law. The framework records converged on-bridge cut-offs once per time, vehicle, and axle, resets the record for each analysis, and excludes unconverged trial iterations and off-bridge forces, and results from any analysis with a non-zero count should be treated as qualitative. The margin is quantified here for the most severe cases of the parametric study: the minimum contact force on the bridge was 0.78 of the static axle load for the heavy truck on the 15 m bridge under level R3 roughness at 10 m/s, 0.60 on the 30 m bridge under level R3 at 30 m/s, and 0.76 under level R2 at 30 m/s (0.47 to 0.57 when the rough approach roads are included), with maxima of 1.4 to 1.6; the commercial vehicle stays within ±4 % of its static load in all cases. The checked roughness cases retained positive total contact forces. This establishes a margin for those profiles only, not for an entire ISO road class. Severe roughness at high speed, short-wavelength defects such as expansion joints and potholes, and lightly loaded axles are the situations in which uplift becomes likely, and they call for a contact model with a tyre enveloping length, a unilateral constraint, and an impact law.

Validation against numerical references only. The three benchmarks are numerical: they establish that the coupling algorithm and

its implementation reproduce reference solutions of the same mathematical model ($R^2 \geq 0.9997$, peak errors of at most 0.14 %), but they do not test the model assumptions (planar beam, point contact, linear suspension, ISO 8608 roughness) against measured bridge or vehicle responses. Field or laboratory validation requires a dataset in which the vehicle parameters (masses, suspension and tyre properties, axle spacing, speed history), the bridge properties, and the road profile are all documented, with calibration data separated from independent validation measurements. No such experimental comparison is included in this study. Green and Cebon (1994) validated a partitioned VBI model against field measurements with an instrumented truck, and Kim et al. (2005) compared a three-dimensional model with field tests. More recently, Gkoktsi et al. (2024) reported full-scale drive-by experiments with modal characterisation of both the vehicle and bridge. Such datasets are needed to assess the modelling assumptions of the present framework.

Deterministic sweeps with Monte Carlo checks. Each simulation is deterministic for a given roughness realisation and traffic draw. Monte Carlo repetitions over 20 roughness and 20 traffic realisations quantify variability for the 30 m bridge (Sections 5.5 and 5.6). The other bridges in the parametric study are represented by single realisations. Distributional results, including response confidence bounds and extreme values, require larger samples, which can be generated with the seeded roughness and traffic models.

Kinematic transfer. The contact input includes the convective contact-velocity term and differentiates roughness along each axle's trajectory. The spatial transfer remains piecewise linear, so slopes change at element boundaries. Mesh and time-step convergence must be checked for damped contact elements, high speeds, and short wavelengths. Prescribed speed changes represent vertical kinematics only: longitudinal braking forces, load transfer, and the associated pitch moment require additional vehicle and bridge DOFs and load channels.

Computational cost. The rebuild-per-step strategy trades speed for robustness and implementation simplicity; its measured cost, the share attributed to model reconstruction, and the saving measured by a persistent bridge domain are reported in Section 6.1.

7. Conclusions

This paper presented an open-source Python framework for vehicle–bridge interaction analysis built on OpenSees. The main contributions are:

1. **A modular VBI framework based on standard FE software.** The bridge and the vehicle are modelled as independent OpenSees finite element subsystems and coupled through an external iterative algorithm. No custom element or change to the OpenSees source code is needed, which makes VBI analysis accessible to the existing OpenSees user base and easy to combine with existing bridge modelling workflows.
2. **Five vehicle model types.** The framework provides five vehicle models of increasing complexity, from a single-axle spring-mass system to a two-axle composite half-car with body pitch, separate axle masses, and independent tyre and suspension components. All models use standard OpenSees elements and are driven by displacement excitation at the contact points.
3. **Numerical verification of the coupling implementation.** The partitioned scheme converges in at most 4–5 iterations per time step under a tight tolerance of 10^{-12} for all benchmarks, in at most 7 iterations when the vehicle mass exceeds the bridge mass by a factor of 24, and in at most 29 iterations, without relaxation, for a vehicle five times heavier than the bridge with a natural frequency three times the bridge's fundamental frequency. Against the published results of Yang et al. (2004a, 2019) for Benchmarks 1 and 2 and an independent reference solution for Benchmark 3, all benchmark responses agree with $R^2 \geq 0.9997$ and peak errors of at most 0.14 %. This is numerical verification; no experimental or field validation is claimed.
4. **A two-parameter characterisation of the decoupled mode.** Parametric studies over four bridge spans, two vehicle classes (more than an order of magnitude apart in mass), six speeds, three roughness levels, and four traffic levels, complemented by a 56-point map over the vehicle-to-bridge mass ratio μ and frequency ratio r and by Monte Carlo repetitions over 20 roughness and 20 traffic realisations, show that the accuracy of the decoupled (moving-load) mode is governed jointly by μ and r, as well as by the response metric. Near frequency tuning, dynamic bridge and vehicle errors can be large even at $\mu = 0.05$, while the peak midspan displacement error stays below 3.5 % on the sampled grid. Response-specific screening targets are given without extrapolation to unsampled ratios or multi-DOF vehicles. Vehicle-class differences in the separate sweeps also involve damping and modal contributions; frequency ratio alone does not isolate their cause.
5. **Open-source release.** The framework source code and vehicle configurations are publicly available through GitHub, together with installation instructions and usage examples.

Future work will extend the framework to three-dimensional analysis with independent wheel paths, add a persistent-domain mode that supports path-dependent (nonlinear) material behaviour for the bridge and the vehicle, add a unilateral contact model with re-contact impact, validate the framework against an instrumented-vehicle field dataset, and add interfaces for online data assimilation in drive-by bridge monitoring.

CRediT authorship contribution statement

Mohammad Talebi-Kalaleh: Writing – original draft, Visualization, Investigation, Formal analysis, Conceptualization. **Qipei Mei:** Writing – review & editing, Validation, Supervision, Methodology, Funding acquisition, Conceptualization.

Declaration of competing interest

The authors declare that they have no known competing financial interests or personal relationships that could have appeared to influence the work reported in this paper.

Given their role as Editorial Board Members, Dr. Qipei Mei had no involvement in the peer review of this article and has no access to information regarding its peer review. Full responsibility for the editorial process for this article was delegated to another journal editor. If there are other authors, they declare that they have no known competing financial interests or personal relationships that could have appeared to influence the work reported in this paper.

Acknowledgment

This research was supported in part by the Natural Sciences and Engineering Research Council of Canada (NSERC) through the Discovery Grant (RGPIN-2022-04160) and Alliance International Grant (ALLRP 597075-2024).

Appendix. OpenSees vehicle model topology

Recorded channels in Table 11 include prescribed contact coordinates and auxiliary penalty-node coordinates; they are not counts of independent physical DOFs. Table 11 summarises the OpenSees node layout, element connectivity, and boundary conditions for each of the five vehicle model types. In all models, axle nodes (contact points) are fully fixed and excited through imposed displacement and velocity

Table 11
OpenSees node and element connectivity for each vehicle model type. Axle nodes are constrained as fixed supports and driven by imposed motion; non-axle nodes are free. Element notation $i \to j$ denotes a spring-dashpot connecting nodes i and j.

Model	ndm	Nodes	Mass assignment	Elements	Notes
one_axle_simple	1	1 (axle, fixed), 2 (body)	m_v at node 2	`zeroLength` 1→2 (k_v, c_v)	1 physical DOF; 2 recorded channels
one_axle_comp	1	1 (contact, fixed), 2 (axle), 3 (body)	m_u at 2, m_s at 3	`zeroLength` 1→2 (k_t, c_t); 2→3 (k_s, c_s)	2 physical DOFs; 3 recorded channels
two_axle_comp1	1	1,2 (axles, fixed); 3,4 (axle masses); 5,6 (body halves)	m_u at 3,4; m_s at 5,6	Tyre: 1→3, 2→4; Susp: 3→ 5,4 →6	4 physical DOFs; 6 recorded channels
two_axle_comp2	2	1,2 (axles, fixed); 5,6 (susp. tops); 7,8 (body at axle x); 9 (CG)	m_v, J_v at 9	Susp: 1→ 5,2 →6 (`twoNodeLink`); Rigid links: 5→ 7 → 9, 6 → 8 →9 (penalty $\sim 10^6 k_s$)	2 physical DOFs; 8 recorded channels
two_axle_comp3	2	1,2 (contacts, fixed); 3,4 (axle masses); 5,6 (susp. tops); 7,8 (body at axle x); 9 (CG)	$m_{u,r}$ at 3, $m_{u,f}$ at 4, m_v, J_v at 9	Tyre: 1→ 3,2 →4; Susp: 3→ 5,4 →6; Rigid links: 5→ 7 → 9, 6 → 8 →9	4 physical DOFs; 10 recorded channels

via the `MultipleSupport` pattern. Non-axle nodes carry lumped mass and are free to respond dynamically. Springs and dashpots are modelled using `zeroLength` elements (1D models) or `twoNodeLink` elements (2D models) with `Elastic` uniaxial materials whose stiffness and damping arguments correspond to the spring constant k and the viscous damping coefficient c, respectively.

For the half-car models with pitch (comp2 and comp3), the rigid-body connection between the CG node (node 9) and the suspension tops (nodes 5, 6) is implemented using intermediate nodes (7, 8) located at the axle x-coordinates but at body height. The `twoNodeLink` elements connecting nodes 7 → 9 and 9 → 8 carry penalty stiffness in all three DOFs (x-translation, y-translation, and rotation), ensuring that the body moves as a rigid bar between the two suspension attachment points. The `zeroLength` elements connecting nodes 5 → 7 and 6 → 8 similarly enforce kinematic compatibility between the suspension tops and the body endpoints. This penalty-based approach avoids the need for multi-point constraints and is compatible with OpenSees' standard analysis procedures.

Framework module pseudocodes

The following pseudocodes summarise the supporting framework modules as step-by-step procedures for readers who prefer the algorithmic form. They restate, in algorithmic notation, the operations described narratively in Sections 3.2, 3.3, 3.4, and 3.7. The main coupled and decoupled procedures appear as Algorithms 1 and 2 in Section 3.

Algorithm 3 Bridge Finite Element Construction and Time Stepping

Require: Span L, support locations, EI, $\bar{m}$, ζ, discretisation N_e, initial conditions $\{w_n, \dot{w}_n, \ddot{w}_n\}$, nodal forces $\mathbf{F}$, time step Δt
Ensure: Bridge response at t_{n+1}: $\{w_{n+1}, \dot{w}_{n+1}, \ddot{w}_{n+1}\}$
`ops.wipe()` ▷ Clear previous model
Define $N_n = N_e + 1$ nodes at spacing $\Delta x = L/N_e$
Apply boundary conditions: pin at first support, roller(s) at remaining
Assign lumped mass: $m_j = \bar{m}\,\Delta x$ (interior nodes), $\bar{m}\,\Delta x/2$ (end nodes)
Define `elasticBeamColumn` elements with A, E, I
Eigenvalue analysis: $\omega_1, \omega_2 \leftarrow$ `ops.eigen`(N_{modes})
Rayleigh damping: $\alpha_M, \beta_K \leftarrow$ solve $\zeta = \frac{1}{2}(\alpha_M/\omega_i + \beta_K \omega_i)$ for $i = 1, 2$
`ops.rayleigh`$(\alpha_M, \beta_K, 0, 0)$
Apply nodal forces $\mathbf{F}$ via `Path` time series and `Plain` load pattern
Set initial conditions: `setNodeDisp`, `setNodeVel`, `setNodeAccel` at each node
Configure `Newmark` integrator ($\gamma = 0.5$, $\beta = 0.25$)
`ops.analyze`$(1, \Delta t)$
Extract updated $\{w_{n+1}, \dot{w}_{n+1}, \ddot{w}_{n+1}\}$ via `nodeDisp`, `nodeVel`, `nodeAccel`

Algorithm 4 Vehicle Finite Element Construction and Time Stepping

Require: Vehicle properties (masses, stiffnesses, dampings), model type, initial conditions, axle displacements $\{u_i\}$ and velocities $\{\dot{u}_i\}$
Ensure: Vehicle response at t_{n+1}, axle reaction forces $\{F_{a,i}\}$
`ops.wipe()`
if model ∈ {one_axle_simple, one_axle_comp} **then**
  Define 1D model (`ndm` = 1)
  Create axle contact node(s), fix all DOFs
  Create body/axle-mass nodes with lumped masses
  Define `zeroLength` spring-dashpot elements (k, c)
else if model ∈ {two_axle_comp2, two_axle_comp3} **then**
  Define 2D model (`ndm` = 2, `ndf` = 3)
  Create axle contact nodes, fix all DOFs
  Create CG node with body mass m_v and rotational inertia J_v
  Create intermediate nodes at axle x-coordinates
  Define `twoNodeLink` suspension elements
  Define penalty links ($k_{\text{pen}} \approx 10^6 k_s$) for rigid-body connection
end if
Apply `MultipleSupport` with `imposedMotion` at each axle node
Prescribe displacement $u_i(t)$ and velocity $\dot{u}_i(t)$ via `Path` time series
Set initial conditions from previous time step
Configure `Newmark` integrator ($\gamma = 0.5$, $\beta = 0.25$)
`ops.analyze`$(1, \Delta t)$
`ops.reactions(-dynamic, -rayleigh)`
$F_{a,i} \leftarrow$ `nodeReaction`(i) for each axle node

Algorithm 5 ISO 8608 Road Roughness Profile Generation

Require: Roughness class coefficient $G_d(n_0)$, spatial range $[x_0, x_{\max}]$, mesh size Δx, bridge span L
Ensure: Roughness profile $r(x_j)$
$\Delta n \leftarrow \min(0.01,\ 1/(2L))$ ▷ Avoid periodicity within bridge span
$n_l \leftarrow \min(0.01,\ \Delta n)$, $n_u \leftarrow 10$ cycles/m
Generate spatial frequency array: $n_k = n_l,\ n_l + \Delta n,\ \ldots,\ n_u$
Compute PSD: $G_d(n_k) = G_d(n_0) \cdot (n_k/n_0)^{-2}$, $n_0 = 0.1$ cycles/m
Compute amplitudes: $A_k = \sqrt{2\, G_d(n_k)\, \Delta n}$
Generate random phases: $\phi_k \sim \mathcal{U}[0, 2\pi]$
Generate position array: $x_j = x_0,\ x_0 + \Delta x,\ \ldots,\ x_{\max}$
for each position x_j **do**
  $r(x_j) = \sum_k A_k \cos(2\pi\, n_k\, x_j + \phi_k)$
end for
Optional: Apply moving-average smoothing (window size w)

Algorithm 6 Vehicle-to-Bridge Force Mapping

Require: Axle positions $\{x_{a,i}\}$, dynamic reaction forces $\{F_{a,i}\}$, static axle weights $\{W_i\}$, bridge node coordinates, bridge span L
Ensure: Equivalent nodal force vector $\mathbf{F}_{\text{inter}}$

```
Initialise F_inter ← 0
for each axle i do
    F_total,i ← W_i + F_a,i                ▷ Static weight + dynamic reaction
    if x_a,i < 0 or x_a,i > L then          ▷ Axle off bridge
        continue
    end if
    if F_total,i ≤ 0 then                  ▷ Wheel uplift: contact force cannot be tensile
        Set F_total,i ← 0 and flag warning
    end if
    Find element [x_j, x_j+1] containing x_a,i
    ξ ← (x_a,i − x_j)/(x_j+1 − x_j)        ▷ Local coordinate
    F_j ← F_j + (1 − ξ) F_total,i
    F_j+1 ← F_j+1 + ξ F_total,i
end for
```

Data availability

The framework source code, vehicle configurations, installation instructions, and usage examples are publicly available in the GitHub repository `OpenSees-VBI-Simulation` (https://github.com/MTalebi/OpenSees-VBI-Simulation).

References

Antolín, P., Zhang, N., Goicolea, J.M., Xia, H., Astiz, M.Á., Oliva, J., 2013. Consideration of nonlinear wheel–rail contact forces for dynamic vehicle–bridge interaction in high-speed railways. J. Sound Vib. 332 (5), 1231–1251. http://dx.doi.org/10.1016/j.jsv.2012.10.022.

Bucinskas, P., Andersen, L.V., 2020. Dynamic response of vehicle–bridge–soil system using lumped-parameter models for structure–soil interaction. Comput. Struct. 238, 106270. http://dx.doi.org/10.1016/j.compstruc.2020.106270.

Cai, C.S., Chen, S.R., 2004. Framework of vehicle–bridge–wind dynamic analysis. J. Wind Eng. Ind. Aerodyn. 92 (7–8), 579–607. http://dx.doi.org/10.1016/j.jweia.2004.03.007.

Cantero, D., 2024. VBI-2D: Road vehicle–bridge interaction simulation tool for MATLAB [software]. GitHub, https://github.com/DanielCanteroNTNU/VBI-2D.

Cantero, D., Hester, D., Brownjohn, J., 2017. Evolution of bridge frequencies and modes of vibration during truck passage. Eng. Struct. 152, 452–464. http://dx.doi.org/10.1016/j.engstruct.2017.09.039.

Cantero, D., Sarwar, M.Z., Malekjafarian, A., Corbally, R., Makki Alamdari, M., Cheema, P., Aggarwal, J., Noh, H.Y., Liu, J., 2024. Numerical benchmark for road bridge damage detection from passing vehicles responses applied to four data-driven methods. Arch. Civ. Mech. Eng. 24 (3), 190. http://dx.doi.org/10.1007/s43452-024-01001-9.

Cheng, Y.S., Au, F.T.K., Cheung, Y.K., 2001. Vibration of railway bridges under a moving train by using bridge-track-vehicle element. Eng. Struct. 23 (12), 1597–1606. http://dx.doi.org/10.1016/S0141-0296(01)00058-X.

Chopra, A.K., 2017. Dynamics of Structures: Theory and Applications To Earthquake Engineering, 5th ed. Pearson, Hoboken, NJ.

Corbally, R., Malekjafarian, A., 2022. A data-driven approach for drive-by damage detection in bridges considering the influence of temperature change. Eng. Struct. 253, 113783. http://dx.doi.org/10.1016/j.engstruct.2021.113783.

Deng, L., Cai, C.S., 2010. Development of dynamic impact factor for performance evaluation of existing multi-girder concrete bridges. Eng. Struct. 32 (1), 21–31. http://dx.doi.org/10.1016/j.engstruct.2009.08.013.

Deng, L., Yu, Y., Zou, Q., Cai, C.S., 2015. State-of-the-art review of dynamic impact factors of highway bridges. J. Bridg. Eng. 20 (5), 04014080. http://dx.doi.org/10.1061/(ASCE)BE.1943-5592.0000672.

Dimitrakopoulos, E.G., Zeng, Q., 2015. A three-dimensional dynamic analysis scheme for the interaction between trains and curved railway bridges. Comput. Struct. 149, 43–60. http://dx.doi.org/10.1016/j.compstruc.2014.12.002.

Elhattab, A., Uddin, N., O'Brien, E., 2016. Drive-by bridge damage monitoring using Bridge Displacement Profile Difference. J. Civ. Struct. Health Monit. 6 (5), 839–850. http://dx.doi.org/10.1007/s13349-016-0203-6.

Enright, B., O'Brien, E.J., 2013. Monte Carlo simulation of extreme traffic loading on short and medium span bridges. Struct. Infrastruct. Eng. 9 (12), 1267–1282. http://dx.doi.org/10.1080/15732479.2012.688753.

Frýba, L., 1999. Vibration of Solids and Structures under Moving Loads, 3rd ed. Emerald Publishing Limited, Leeds, http://dx.doi.org/10.1680/vosasuml.35393.

Gao, K., Gu, J., Chen, Z., Zhang, H., Kong, X., Cai, C., Wu, G., 2026. Non-contact vehicle weigh-in-motion (WIM) for bridge health monitoring: A review. Measurement 290, 122919. http://dx.doi.org/10.1016/j.measurement.2026.122919.

Gkoktsi, K., Bono, F., Tirelli, D., 2024. Effectiveness of drive-by monitoring in short-span bridges: A real-scale experimental evaluation. Struct. Control. Health Monit. 2024, 3509941. http://dx.doi.org/10.1155/2024/3509941.

González, A., 2010. Vehicle-bridge dynamic interaction using finite element modelling. In: Moratal, D. (Ed.), Finite Element Analysis. IntechOpen, London, http://dx.doi.org/10.5772/10235.

González, A., O'Brien, E.J., Li, Y.Y., Cashell, K., 2008. The use of vehicle acceleration measurements to estimate road roughness. Veh. Syst. Dyn. 46 (6), 483–499. http://dx.doi.org/10.1080/00423110701485050.

González, A., O'Brien, E.J., McGetrick, P.J., 2012. Identification of damping in a bridge using a moving instrumented vehicle. J. Sound Vib. 331 (18), 4115–4131. http://dx.doi.org/10.1016/j.jsv.2012.04.019.

Green, M.F., Cebon, D., 1994. Dynamic response of highway bridges to heavy vehicle loads: Theory and experimental validation. J. Sound Vib. 170 (1), 51–78. http://dx.doi.org/10.1006/jsvi.1994.1046.

Hester, D., González, A., 2017. A discussion on the merits and limitations of using drive-by monitoring to detect localised damage in a bridge. Mech. Syst. Signal Process. 90, 234–253. http://dx.doi.org/10.1016/j.ymssp.2016.12.012.

Huang, D., Wang, T.L., Shahawy, M., 1992. Impact analysis of continuous multigirder bridges due to moving vehicles. J. Struct. Eng. 118 (12), 3427–3443. http://dx.doi.org/10.1061/(ASCE)0733-9445(1992)118:12(3427).

International Organization for Standardization, 2016. ISO 8608:2016 – Mechanical Vibration – Road Surface Profiles – Reporting of Measured Data. ISO, Geneva.

Irawan, J., Kim, C.W., Cantero, D., Yokoyama, T., 2025. Revised virtual axle method for damage detection using bridge weigh-in-motion systems. J. Civ. Struct. Health Monit. 15 (8), 3731–3742. http://dx.doi.org/10.1007/s13349-025-01013-w.

Keenahan, J., O'Brien, E.J., McGetrick, P.J., González, A., 2014. The use of a dynamic truck–trailer drive-by system to monitor bridge damping. Struct. Health Monit. 13 (2), 143–157. http://dx.doi.org/10.1177/1475921713513974.

Kim, C.W., Kawatani, M., 2008. Pseudo-static approach for damage identification of bridges based on coupling vibration with a moving vehicle. Struct. Infrastruct. Eng. 4 (5), 371–379. http://dx.doi.org/10.1080/15732470701270082.

Kim, C.W., Kawatani, M., Kim, K.B., 2005. Three-dimensional dynamic analysis for bridge–vehicle interaction with roadway roughness. Comput. Struct. 83 (19–20), 1627–1645. http://dx.doi.org/10.1016/j.compstruc.2004.12.004.

Kim, C.W., Kawatani, M., Konaka, S., Kitaura, R., 2011. Seismic responses of a highway viaduct considering vehicles of design live load as dynamic system during moderate earthquakes. Struct. Infrastruct. Eng. 7 (7–8), 523–534. http://dx.doi.org/10.1080/15732479.2010.493339.

Kong, X., Cai, C.S., Kong, B., 2016. Numerically extracting bridge modal properties from dynamic responses of moving vehicles. J. Eng. Mech. 142 (6), 04016025. http://dx.doi.org/10.1061/(ASCE)EM.1943-7889.0001033.

Law, S.S., Zhu, X.Q., 2004. Dynamic behavior of damaged concrete bridge structures under moving vehicular loads. Eng. Struct. 26 (9), 1279–1293. http://dx.doi.org/10.1016/j.engstruct.2004.04.007.

Law, S.S., Zhu, X.Q., 2005. Bridge dynamic responses due to road surface roughness and braking of vehicle. J. Sound Vib. 282 (3–5), 805–830. http://dx.doi.org/10.1016/j.jsv.2004.03.032.

Li, J., Zhu, X., Law, S.S., Samali, B., 2019. Indirect bridge modal parameters identification with one stationary and one moving sensors and stochastic subspace identification. J. Sound Vib. 446, 1–21. http://dx.doi.org/10.1016/j.jsv.2019.01.024.

Lin, C.W., Yang, Y.B., 2005. Use of a passing vehicle to scan the fundamental bridge frequencies: An experimental verification. Eng. Struct. 27 (13), 1865–1878. http://dx.doi.org/10.1016/j.engstruct.2005.06.016.

Lydon, M., Taylor, S.E., Robinson, D., Mufti, A., O'Brien, E.J., 2016. Recent developments in bridge weigh in motion (B-WIM). J. Civ. Struct. Health Monit. 6 (1), 69–81. http://dx.doi.org/10.1007/s13349-015-0119-6.

Malekjafarian, A., Corbally, R., Gong, W., 2022. A review of mobile sensing of bridges using moving vehicles: Progress to date, challenges and future trends. Structures 44, 1466–1489. http://dx.doi.org/10.1016/j.istruc.2022.08.075.

Malekjafarian, A., McGetrick, P.J., O'Brien, E.J., 2015. A review of indirect bridge monitoring using passing vehicles. Shock. Vib. 2015, 286139. http://dx.doi.org/10.1155/2015/286139.

Malekjafarian, A., O'Brien, E.J., 2017. On the use of a passing vehicle for the estimation of bridge mode shapes. J. Sound Vib. 397, 77–91. http://dx.doi.org/10.1016/j.jsv.2017.02.051.

Matarazzo, T.J., Kondor, D., Milardo, S., Eshkevari, S.S., Santi, P., Pakzad, S.N., Buehler, M.J., Ratti, C., 2022. Crowdsourcing bridge dynamic monitoring with smartphone vehicle trips. Commun. Eng. 1 (1), 29. http://dx.doi.org/10.1038/s44172-022-00025-4.

Matarazzo, T.J., Santi, P., Pakzad, S.N., Carter, K., Ratti, C., Moaveni, B., Osgood, C., Jacob, N., 2018. Crowdsensing framework for monitoring bridge vibrations using moving smartphones. Proc. IEEE 106 (4), 577–593. http://dx.doi.org/10.1109/JPROC.2018.2808759.

McKenna, F., 2011. OpenSees: A framework for earthquake engineering simulation. Comput. Sci. Eng. 13 (4), 58–66. http://dx.doi.org/10.1109/MCSE.2011.66.

Mei, Q., Gül, M., Boay, M., 2019. Indirect health monitoring of bridges using Mel-frequency cepstral coefficients and principal component analysis. Mech. Syst. Signal Process. 119, 523–546. http://dx.doi.org/10.1016/j.ymssp.2018.10.006.

Mei, Q., Gül, M., Shirzad-Ghaleroudkhani, N., 2021. Towards smart transportation system: A vehicle scanning method for bridge health monitoring. Computer-Aided Civ. Infrastruct. Eng. 36 (5), 614–630. http://dx.doi.org/10.1111/mice.12650.

Montenegro, P.A., Neves, S.G.M., Calçada, R., Tanabe, M., Sogabe, M., 2015. Wheel–rail contact formulation for analyzing the lateral train–structure dynamic interaction. Comput. Struct. 152, 200–214. http://dx.doi.org/10.1016/j.compstruc.2015.01.004.

Moses, F., 1979. Weigh-in-motion system using instrumented bridges. Transp. Eng. J. ASCE 105 (3), 233–249. http://dx.doi.org/10.1061/TPEJAN.0000783.

Neves, S.G.M., Azevedo, A.F.M., Calçada, R., 2012. A direct method for analyzing the vertical vehicle–structure interaction. Eng. Struct. 34, 414–420. http://dx.doi.org/10.1016/j.engstruct.2011.10.010.

Newmark, N.M., 1959. A method of computation for structural dynamics. J. Eng. Mech. Div. 85 (3), 67–94. http://dx.doi.org/10.1061/jmcea3.0000098.

O'Brien, E.J., Enright, B., 2011. Modeling same-direction two-lane traffic for bridge loading. Struct. Saf. 33 (4–5), 296–304. http://dx.doi.org/10.1016/j.strusafe.2011.04.004.

O'Brien, E.J., Keenahan, J., 2015. Drive-by damage detection in bridges using the apparent profile. Struct. Control. Health Monit. 22 (5), 813–825. http://dx.doi.org/10.1002/stc.1721.

O'Brien, E.J., McGetrick, P.J., González, A., 2014. A drive-by inspection system via vehicle moving force identification. Smart Struct. Syst. 13 (5), 821–848. http://dx.doi.org/10.12989/sss.2014.13.5.821.

O'Brien, E.J., Quilligan, M.J., Karoumi, R., 2006. Calculating an influence line from direct measurements. Proc. Inst. Civ. Eng. Bridg. Eng. 159 (1), 31–34. http://dx.doi.org/10.1680/bren.2006.159.1.31.

Paul, D., Roy, K., 2023. Application of bridge weigh-in-motion system in bridge health monitoring: A state-of-the-art review. Struct. Health Monit. 22 (6), 4194–4232. http://dx.doi.org/10.1177/14759217231154431.

Sadeghi Eshkevari, S., Matarazzo, T.J., Pakzad, S.N., 2020a. Bridge modal identification using acceleration measurements within moving vehicles. Mech. Syst. Signal Process. 141, 106733. http://dx.doi.org/10.1016/j.ymssp.2020.106733.

Sadeghi Eshkevari, S., Matarazzo, T.J., Pakzad, S.N., 2020b. Simplified vehicle–bridge interaction for medium to long-span bridges subject to random traffic load. J. Civ. Struct. Health Monit. 10 (4), 693–707. http://dx.doi.org/10.1007/s13349-020-00413-4.

Sarwar, M.Z., Cantero, D., 2021. Deep autoencoder architecture for bridge damage assessment using responses from several vehicles. Eng. Struct. 246, 113064. http://dx.doi.org/10.1016/j.engstruct.2021.113064.

Shirzad-Ghaleroudkhani, N., Gül, M., 2020. Inverse filtering for frequency identification of bridges using smartphones in passing vehicles: Fundamental developments and laboratory verifications. Sensors 20 (4), 1190. http://dx.doi.org/10.3390/s20041190.

Stoura, C.D., Dimitrakopoulos, E.G., 2020a. Additional damping effect on bridges because of vehicle-bridge interaction. J. Sound Vib. 476, 115294. http://dx.doi.org/10.1016/j.jsv.2020.115294.

Stoura, C.D., Dimitrakopoulos, E.G., 2020b. MDOF extension of the Modified Bridge System method for vehicle–bridge interaction. Nonlinear Dynam. 102 (4), 2103–2123. http://dx.doi.org/10.1007/s11071-020-06022-6.

Stoura, C.D., Dimitrakopoulos, E.G., 2020c. A Modified Bridge System method to characterize and decouple vehicle–bridge interaction. Acta Mech. 231 (9), 3825–3845. http://dx.doi.org/10.1007/s00707-020-02699-3.

Stoura, C.D., Paraskevopoulos, E., Dimitrakopoulos, E.G., Natsiavas, S., 2021. A Dynamic Partitioning Method to solve the vehicle-bridge interaction problem. Comput. Struct. 251, 106547. http://dx.doi.org/10.1016/j.compstruc.2021.106547.

Talebi-Kalaleh, M., Mei, Q., 2023. A mobile sensing framework for bridge modal identification through an inverse problem solution procedure and moving-window time series models. Sensors 23 (11), 5154. http://dx.doi.org/10.3390/s23115154.

Talebi-Kalaleh, M., Mei, Q., 2024. Damage detection in bridge structures through compressed sensing of crowdsourced smartphone data. Struct. Control. Health Monit. 2024, 5436675. http://dx.doi.org/10.1155/2024/5436675.

Xia, H., Zhang, N., 2005. Dynamic analysis of railway bridge under high-speed trains. Comput. Struct. 83 (23–24), 1891–1901. http://dx.doi.org/10.1016/j.compstruc.2005.02.014.

Xu, Y.L., Guo, W.H., 2003. Dynamic analysis of coupled road vehicle and cable-stayed bridge systems under turbulent wind. Eng. Struct. 25 (4), 473–486. http://dx.doi.org/10.1016/S0141-0296(02)00188-8.

Yang, Y.B., Li, Y.C., Chang, K.C., 2014. Constructing the mode shapes of a bridge from a passing vehicle: A theoretical study. Smart Struct. Syst. 13 (5), 797–819. http://dx.doi.org/10.12989/sss.2014.13.5.797.

Yang, Y.B., Lin, C.W., Yau, J.D., 2004a. Extracting bridge frequencies from the dynamic response of a passing vehicle. J. Sound Vib. 272 (3–5), 471–493. http://dx.doi.org/10.1016/S0022-460X(03)00378-X.

Yang, Y.B., Wang, Z.L., Shi, K., Xu, H., Wu, Y.T., 2020. State-of-the-art of vehicle-based methods for detecting various properties of highway bridges and railway tracks. Int. J. Struct. Stab. Dyn. 20 (13), 2041004. http://dx.doi.org/10.1142/S0219455420410047.

Yang, Y.B., Yang, J.P., 2018. State-of-the-art review on modal identification and damage detection of bridges by moving test vehicles. Int. J. Struct. Stab. Dyn. 18 (2), 1850025. http://dx.doi.org/10.1142/S0219455418500256.

Yang, Y.B., Yau, J.D., 1997. Vehicle–bridge interaction element for dynamic analysis. J. Struct. Eng. 123 (11), 1512–1518. http://dx.doi.org/10.1061/(ASCE)0733-9445(1997)123:11(1512).

Yang, Y.B., Yau, J.D., Wu, Y.S., 2004b. Vehicle–Bridge Interaction Dynamics: With Applications to High-Speed Railways. World Scientific, Singapore, http://dx.doi.org/10.1142/5541.

Yang, Y.B., Zhang, B., Qian, Y., Wu, Y., 2018. Contact-point response for modal identification of bridges by a moving test vehicle. Int. J. Struct. Stab. Dyn. 18 (5), 1850073. http://dx.doi.org/10.1142/S0219455418500736.

Yang, Y.B., Zhang, B., Wang, T., Xu, H., Wu, Y., 2019. Two-axle test vehicle for bridges: Theory and applications. Int. J. Mech. Sci. 152, 51–62. http://dx.doi.org/10.1016/j.ijmecsci.2018.12.043.

Yin, X., Fang, Z., Cai, C.S., Deng, L., 2010. Non-stationary random vibration of bridges under vehicles with variable speed. Eng. Struct. 32 (8), 2166–2174. http://dx.doi.org/10.1016/j.engstruct.2010.03.019.

Yu, Y., Cai, C.S., Deng, L., 2016. State-of-the-art review on bridge weigh-in-motion technology. Adv. Struct. Eng. 19 (9), 1514–1530. http://dx.doi.org/10.1177/1369433216655922.

Zeng, Q., Dimitrakopoulos, E.G., 2016. Seismic response analysis of an interacting curved bridge–train system under frequent earthquakes. Earthq. Eng. Struct. Dyn. 45 (7), 1129–1148. http://dx.doi.org/10.1002/eqe.2699.

Zhai, W., Han, Z., Chen, Z., Ling, L., Zhu, S., 2019. Train–track–bridge dynamic interaction: A state-of-the-art review. Veh. Syst. Dyn. 57 (7), 984–1027. http://dx.doi.org/10.1080/00423114.2019.1605085.

Zhai, W., Xia, H., Cai, C., Gao, M., Li, X., Guo, X., Zhang, K., 2013. High-speed train–track–bridge dynamic interactions – part I: Theoretical model and numerical simulation. Int. J. Rail Transp. 1 (1–2), 3–24. http://dx.doi.org/10.1080/23248378.2013.791498.

Zhao, H., Uddin, N., O'Brien, E.J., Shao, X., Zhu, P., 2014. Identification of vehicular axle weights with a bridge weigh-in-motion system considering transverse distribution of wheel loads. J. Bridg. Eng. 19 (3), 04013008. http://dx.doi.org/10.1061/(ASCE)BE.1943-5592.0000533.

Zhu, X.Q., Law, S.S., 2002. Dynamic load on continuous multi-lane bridge deck from moving vehicles. J. Sound Vib. 251 (4), 697–716. http://dx.doi.org/10.1006/jsvi.2001.3996.

Zhu, X.Q., Law, S.S., 2015. Structural health monitoring based on vehicle–bridge interaction: Accomplishments and challenges. Adv. Struct. Eng. 18 (12), 1999–2015. http://dx.doi.org/10.1260/1369-4332.18.12.1999.

Zhu, X.Q., Law, S.S., 2016. Recent developments in inverse problems of vehicle–bridge interaction dynamics. J. Civ. Struct. Health Monit. 6 (1), 107–128. http://dx.doi.org/10.1007/s13349-016-0155-x.

Zhu, M., McKenna, F., Scott, M.H., 2018. OpenSeesPy: Python library for the OpenSees finite element framework. SoftwareX 7, 6–11. http://dx.doi.org/10.1016/j.softx.2017.10.009.